

Heavy ion collisions with non-equilibrium Dirac-Brueckner mean fields

T. Gaitanos^a, C. Fuchs^b, H. H. Wolter^a

^a*Sektion Physik, Universität München, D-85748 Garching, Germany*

^b*Institut für Theoretische Physik, Universität Tübingen, D-72076 Tübingen,
Germany*

Abstract

The influence of realistic interactions on the reaction dynamics in intermediate energy heavy ion collisions is investigated. The mean field in relativistic transport calculations is derived from microscopic Dirac-Brueckner (DB) self-energies, taking non-equilibrium effects, in particular the anisotropy of the local phase space configurations, into account. Thus this approach goes beyond the local density approximation. A detailed analysis of various in-plane and out-of-plane flow observables is presented for Au on Au reactions at incident energies ranging from 250 to 800 A.MeV and the results are compared to recent measurements of the FOPI collaboration. An overall good agreement with in-plane flow data and a reasonable description of the out-of-plane emission is achieved. For these results the intrinsic momentum dependence of the non-equilibrium mean fields is important. On the other hand, the local density approximation with the same underlying DB forces as well as a standard non-linear version of the $\sigma\omega$ model are less successful in describing the present data. This gives evidence of the applicability of self energies derived from the DB approach to nuclear matter also far from saturation and equilibrium.

Key words: Dirac-Brueckner, non-equilibrium mean field, relativistic BUU, Au+Au, E=250–800 MeV/nucleon reaction, nucleon flow.

PACS numbers: **25.75.-q**, 25.60.Gc, 25.70.Mn,

1 Introduction

Heavy ion physics at intermediate energies, i.e. up to some GeV bombarding energy per nucleon, open the possibility to investigate the nuclear equation-of-state (EOS) under extreme conditions. In contrast to the studies of finite nuclei which mainly yield information about the regions close to the saturation point of nuclear matter, in heavy ion collisions the systems undergoes a violent evolution from highly compressed to decompressed matter. However, after more than a decade of extensive efforts the equation-of-state is still a question of current debate.

On the other hand, the development of modern nuclear structure physics provided successful tools to handle the nuclear many-body problem for equilibrated systems. Especially, the relativistic Dirac-Brueckner Hartree-Fock (DB) approach [1–6] turned out to be a significant advance in the understanding of the nuclear matter saturation mechanism. This approach is essentially parameter free since it is based on a model for the bare NN interaction given by boson exchange potentials [7]. At present, however, because of its high complexity the DB approach is restricted to the description of nuclear matter or light nuclei. It is tempting, however, to take a benefit of these results also in other nuclear systems. There have been successful attempts to realize such a program with respect to the description of finite nuclei [8–10]. Thus it is a natural step to continue this approach to heavy ion physics [11].

However, ground state nuclear matter results have to be used carefully in the description of heavy ion reactions since here the system most of the time is far away from global or even local thermodynamical equilibrium [12]. As a consequence the local density approximation (LDA) is not well adapted to describe the phase space in heavy ion collisions and problems arise when con-

clusions about the equilibrium EOS are drawn from heavy ion collisions in this approximation. Instead, the anisotropy of the momentum configuration should be taken into account while, in contrast, the LDA refers to equilibrated nuclear matter, i.e. to one Fermi sphere in momentum space possibly with a diffuse surface if a finite temperature is included. Thus, the LDA only includes the monopole moment of the local momentum configuration and is a poor approximation in the case of non-equilibrium situations. One way to go beyond this approximation is the so called local phase space configuration approximation (LCA) [11–13] which approximates the system locally by two Fermi spheres, i.e. by two interpenetrating currents of nuclear matter also called the colliding nuclear matter configuration. It is seen in actual calculations that this configuration describes fairly well the local phase space evolution over a large part of a heavy ion reaction [12].

The most established models for the theoretical description of the phase space evolution of the colliding nuclei are transport theories leading to a semi-classical kinetic equation of a Boltzmann type for the one-body density of the system, known as Boltzmann-Uehling-Uhlenbeck, Vlasov-Uehling-Uhlenbeck, or Landau-Vlasov equations (BUU, VUU, LV) [14,15]. In recent years it has been found that even in stationary nuclear structure calculations a relativistic formalism [16,17] appears to be superior to a non-relativistic one since the occurrence of large scalar and vector fields leads to new mechanisms of saturation. Thus relativistic transport theories have been developed leading to the relativistic RBUU or RLV equation [18–21]. These approaches are formulated in the framework of a relativistic hadronic field theory (Quantum Hadron Dynamics, (QHD) [16]) which includes baryons and mesons, and naturally contains large scalar and vector fields.

The derivation of transport equations usually starts from the Schwinger–Keldysh formalism of non-equilibrium Green functions and can be found, e.g., in Refs. [20,22,23]. A transport equation in the T-matrix approximation was

derived by Botermans and Malfliet [23] and thus the connection to the DB theory of nuclear matter was achieved. In this formulation it becomes clear that both, the mean field as well as the in-medium cross section are given through the T-matrix. To determine these quantities in a fully consistent way the equations for the effective interaction, i.e. the Bethe–Salpeter equation, has to be solved simultaneously with the kinetic equation. This, however, is a problem too complex to solve. However, an approximate treatment can be performed within the spirit of the LCA, i.e. in a stationary colliding nuclear matter approximation. Sehn, Fuchs and Wolter developed a procedure to construct approximately Dirac–Brueckner self-energies as well as in-medium cross sections for colliding nuclear matter, i.e for two–Fermi–ellipsoid momentum configurations [24–26] starting from a parametrisation of Dirac–Brueckner ground state results [2]. These non–equilibrium self-energies account for the full dependence of the specific momentum configuration and they include the correlations of the relativistic in-medium T-matrix.

Of course, it has been realized earlier that the reaction dynamics cannot be understood only in terms of a compression/decompression scenario (for an overview see e.g. [27]) and that dynamic momentum dependent effects plays an essential role. Hence, repulsive momentum dependent interactions have been introduced phenomenologically [28–30]. Thus the description of intermediate energy [31] flow data was considerably improved [32,33]. Also in-medium cross sections have been derived from the relativistic [3,34] and non-relativistic G-matrix [35,36]. However, the dependence of these quantities on non–equilibrium momentum configurations, i.e. beyond the LDA, has been poorly investigated. The most complete treatment was done by the Tübingen group where fields and cross sections were calculated from a non-relativistic G-matrix [37] based on the Reid-soft-core interaction taking also two-Fermi-sphere configurations into account [36]. It turned out that standard observables of heavy ion collisions as, e.g. the transverse flow or the balance energy, react

quite sensitively to non-equilibrium effects of such realistic forces [38–40]. A comparison with experiment shows a satisfying agreement in general which in some cases seems to be even better than with the phenomenological, e.g. Skyrme, forces [31,41]. However, the non-relativistic G-matrix calculations are not able to reproduce the correct saturation properties of nuclear matter and thus a relativistic approach seems preferable.

In the present work we perform a detailed comparison of RLV calculations with non-equilibrium Dirac-Brueckner mean fields with recent flow data measured by the FOPI Collaboration at GSI [27,31,42–45] for the system *Au* on *Au*. The incident energy ranges from 250 to 800 A.MeV. These data are much more exclusive than, e.g., the previous Steamer Chamber data [46] since they are obtained with a high centrality resolution and a mass selection for light fragments. The energy range is suited in particular to test the relativistic Brueckner approach since the optical potential [47] is reasonably reproduced up to energies around 600–800 MeV by the DB model [2,5]. In Ref. [11] results for transverse flow for 400 A.MeV have already been reported. These investigations are now extended to other energies and a wider range of observables, i.e. fragment flow, squeeze-out etc.

The paper is organized as follows: To set up the context of the present discussion and to make the work self-contained the basic steps which lead to the transport equation are briefly reviewed in section 2. In section 3 we discuss the general structure of the relativistic self-energy in non-equilibrium, i.e. colliding nuclear matter, as it can be applied in transport calculations. Section 4 presents more details on the models used in the present work and section 5 gives details on the numerical implementation of this program. Finally in section 6 results for *Au* on *Au* reactions at 250, 400, 600 and 800 A.MeV are presented for the various approaches: On the one hand, the DB mean field applied in the local configuration approximation (called DB/LCA) and in the local density approximation, i.e. neglecting the non-equilibrium features of the

phase space, (called DB/LDA) to examine the influence of non-equilibrium effects. We also compare to the NL2 parametrisation of the non-linear $\sigma\omega$ -model as an example of a widely used phenomenological force. Finally we draw conclusions in section 7.

2 Transport equation

The derivation of a kinetic equation frequently starts from the real time Schwinger–Keldysh formalism [48] of Green functions. Such derivations have been given in refs. [22,23,49–51]. We very briefly review the relevant steps here. One obtains a matrix \underline{G} of Green functions, (anti-) chronologically ordered Green functions and correlation functions $G^{>,<}$. The correlation functions are defined as $G^>(1, 1') = -i \langle \Psi(1)\bar{\Psi}(1') \rangle$ and $G^<(1, 1') = i \langle \bar{\Psi}(1)\Psi(1') \rangle$ using the notation $\eta = (t_\eta, \mathbf{x}_\eta)$. The quantity of interest is $G^<$ because in the limit $t_1 = t'_1$ it corresponds to a density. The Dyson equation in non-equilibrium is given as a matrix equation

$$D(1, 1')\underline{G}(1, 1') = \underline{\delta}(1 - 1') + \int d2\underline{\Sigma}(1, 2)\underline{G}(2, 1') \quad , \quad (1)$$

with the definition $D(1, 1') \equiv (i\gamma_\mu\partial_1^\mu - M)\underline{\delta}(1 - 1')$. The matrix of self-energies $\underline{\Sigma}$ in Eq. (1) contains all higher order correlations originating from the higher order Green functions of the Schwinger–Keldysh hierarchy. In the Dirac–Brueckner approach the hierarchy is truncated at the two–body level by summing all two–body ladder correlations in the T–matrix which obeys a Bethe–Salpeter equation [1,2]. The self-energy is obtained from the T–matrix, taking, however, the different time orderings into account. To determine the effective interaction, i.e. the T-matrix, as the solution of the Bethe-salpeter equation for general non-equilibrium phase space configurations is an extremely complex and yet unsolved problem. Thus suitable approximations have to be found, which is the object of the next section.

A kinetic equation for the correlation function $G^<$ is obtained by subtracting from the Dyson equation (1) its adjoint. A Wigner transformation then allows to represent the kinetic equation in phase space, i.e. $x-p$ -space, rather than in coordinate space. An essential step is the truncation of the gradient expansion of the Wigner transform of products retaining only terms of first order in \hbar , which neglect memory terms. The self-energy, Eq. (1), is decomposed into scalar and vector parts

$$\Sigma^+ = \Sigma_s^+ - \gamma^\mu \Sigma_\mu^+ \quad (2)$$

and the real part of Σ^+ is used to define effective masses and kinetic momenta

$$m^* = M + Re\Sigma_s^+(x, p) \quad , \quad p_\mu^* = p_\mu + Re\Sigma_\mu^+(x, p) \quad (3)$$

of the dressed particles in the nuclear medium. Σ^+ is the retarded self energy constructed by the difference of the corresponding correlation functions $G^\pm(1, 1') = \theta(\pm(t_1 - t_{1'})) [G^>(1, 1') - G^<(1, 1')] [4]$. The Dirac structure of the correlation functions $G^{>,<}$ can be separated off by a decomposition into a scalar spectral function a , a scalar distribution function F and the projector onto positive energy states. In spin and isospin saturated systems the functions $G^{>,<}$ are then of similar form as in equilibrated nuclear matter [1,2]

$$G^<(x, p) = i (\not{p}^* + m^*) a(x, p) F(x, p) \quad (4)$$

$$G^>(x, p) = -i (\not{p}^* + m^*) a(x, p) [1 - F(x, p)] \quad (5)$$

In an essential, but little investigated approximation the spectral properties of the baryons are treated in the quasiparticle approximation which is valid in the limit of a small imaginary part of the self energy ($Im\Sigma^+ \ll Re\Sigma^+$). The spectral function then reduces to the mass shell constraint $a(x, p) = 2\pi\delta(p^{*2} - m^{*2}) 2\Theta(p_0^*)$ which sets the energy on the mass shell $p_0^* = E^*(\mathbf{p}) = \sqrt{\mathbf{p}^{*2} + m^{*2}}$. Thus, the number of variables of the distribution function $F(x, p)$

is reduced from eight to seven

$$a(x, p)F(x, P) = 2\pi\delta[p^{*2} - m^{*2}]2\Theta(p_0^*)f(x, \mathbf{p}) \quad (6)$$

which simplifies considerably practical implementations.

Usually the kinetic equation is treated in the Hartree approximation which implies to neglect the explicit momentum dependence of the mean field, i.e. $Re\Sigma^+ = Re\Sigma_H^+(x)$. Then the resulting kinetic equation can be completely be formulated in terms of kinetic momenta instead of canonical momenta [4,18]

$$\begin{aligned} & \left[p^{*\mu} \partial_\mu^x + (p_\nu^* F^{\mu\nu} + m^* \partial_x^\mu m^*) \partial_\mu^{p^*} \right] (aF)(x, p^*) \\ &= \frac{1}{2} \int \frac{d^4 p_2}{(2\pi)^4} \frac{d^4 p_3}{(2\pi)^4} \frac{d^4 p_4}{(2\pi)^4} a(x, p) a(x, p_2) a(x, p_3) a(x, p_4) W(pp_2|p_3p_4) \\ & \times (2\pi)^4 \delta^4(p + p_2 - p_3 - p_4) [F(x, p_3)F(x, p_4) (1 - F(x, p)) (1 - F(x, p_2)) \\ & - F(x, p)F(x, p_2) (1 - F(x, p_3)) (1 - F(x, p_4))] \quad . \end{aligned} \quad (7)$$

Eq. (7) resembles the well known transport equation of a Boltzmann–Uehling–Uhlenbeck type. The left hand side is a drift term driven by the mean field via the kinetic momenta p^* , the field strength tensor $F^{\mu\nu}(x) = \partial_x^\nu Re\Sigma_H^{+\mu}(x) - \partial_x^\mu Re\Sigma_H^{+\nu}(x)$, and the effective mass m^* . The right hand side is a collision integral which contains the transition rate W or equally the in–medium cross section given by $(p^* + p_2^*)^2 \frac{d\sigma}{d\Omega}(p, p_2) = W(pp_2|p_3p_4)$. As discussed in the introduction in a fully consistent approach the later is given by the square of the non–equilibrium T–matrix [4,26,36]. However, in the present work we concentrate on non-equilibrium features of the mean field and apply a phenomenological parametrisation of the cross section [52].

3 Colliding nuclear matter approximation

Here we discuss approximations to construct the non-equilibrium self-energy for the two Fermi–sphere or colliding nuclear matter system [25]. This will be

used in the transport calculations in the Local (phase space) Configuration Approximation (LCA). In this section we only consider the structure of the self-energy in colliding nuclear matter which is independent of the particular choice of the nuclear interaction.

3.1 Local density approximation

The mean field is commonly determined in the local density approximation, i.e. it is taken as that of ground state nuclear matter (n.m.) at the respective total density

$$Re\Sigma^+(x, p) = Re\Sigma^{(n.m.)}(p_F(x), p) \quad (8)$$

$$p_F(x) = \left(\frac{3}{2}\pi^2\rho_B(x)\right)^{\frac{1}{3}} \quad (9)$$

$$\rho_B(x) = 4 \int \frac{d^3p}{(2\pi)^3} f(x, \mathbf{p}) \quad (10)$$

Here the mean field $\Sigma^{(n.m.)}$ has been taken from different sources. In non-relativistic applications Skyrme forces are used [28,38] or the mean field has been obtained microscopically from the G-matrix [37,38]. In relativistic treatments, Eq. (7), the mean field is usually determined in a Hartree approximation in the framework of the $\sigma\omega$ -model [16], in particular of its non-linear extensions [19,53–55]. Calculations with momentum dependent fields have been performed in Refs. [32] with self-energies of Hartree-Fock form [30] and fitted to the energy dependence of the empirical nucleon-nucleus optical potential [47]. A similar procedure is applied in non-relativistic calculations when momentum dependent Skyrme forces are used [28]. However, all these represent the mean field of equilibrated nuclear matter.

3.2 Local configuration approximation

In the *local (phase space) configuration approximation* (LCA) the self energies are parameterized for a phase space configuration of two inter-penetrating currents of nuclear matter, so called colliding nuclear matter. The covariant momentum distributions of the currents are given by Fermi ellipsoids [25,26] and shown in Fig. 1. A unique parametrisation of such a configuration is based on five Lorentz invariants which are naturally chosen as the Fermi momenta of the currents and their relative velocity. In a transport calculation these parameters are determined from the vector currents which are obtained from a decomposition of the phase space distribution into contributions from projectile (1) and target (2), i.e. $f^{(12)} = f^{(1)} + f^{(2)}$. The Fermi momenta are defined in the rest frames of the respective currents by the invariant rest densities $\rho_0^{(i)}$

$$j_\mu^{(i)}(x) = 4 \int \frac{d^3p}{(2\pi)^3} \frac{p_\mu^*}{E^*} f^{(i)}(x, \mathbf{p}) \quad , \quad i = 1, 2 \quad (11)$$

$$\rho_0^{(i)}(x) = \sqrt{j_\mu^{(i)}(x) j^{(i)\mu}(x)} \quad . \quad (12)$$

The current four-velocities $u_\mu^{(i)} = (u_0^{(i)}, \mathbf{u}^{(i)})$ and the relative velocity \mathbf{v}_{rel} are defined as

$$u_\mu^{(i)}(x) = j_\mu^{(i)}(x) / \rho_0^{(i)}(x) \quad (13)$$

$$\mathbf{v}_{\text{rel}}(x) = \frac{u_0^{(2)} \mathbf{u}^{(1)} - u_0^{(1)} \mathbf{u}^{(2)}}{u_\mu^{(1)} u^{(2)\mu}} \quad . \quad (14)$$

One should note that the relative velocity, Eq. (14), is not a space-like vector but each component remains invariant under Lorentz transformations. In any reference frame, e.g. the center-of-mass (c.m.) frame of the currents, one component of \mathbf{v}_{rel} is sufficient to characterize the configuration and the remaining two parameters are used to fix the reference frame. Thus in the following we write simply v_{rel} and refer to the c.m. frame of the currents. The local density approximation is recovered in the limit of a vanishing relative velocity

$LCA \xrightarrow{v_{\text{rel}} \rightarrow 0} LDA$.

In the LDA, instead, one would obtain the density and the streaming velocity of the total system (index 12) as

$$\rho_0^{(12)} = \sqrt{j_\mu^{(12)} j^{\mu(12)}} = \rho_B^{(12)}|_{\text{c.m.}} \quad , \quad j_\mu^{(12)} = u_\mu^{(12)} \rho_0^{(12)} \quad . \quad (15)$$

In the c.m. frame which is the natural reference frame in colliding nuclear matter the spatial components vanish for the total vector current $j_\mu^{(12)} = (\rho_0^{(12)}, \mathbf{0})$ and for the total streaming velocity $u_\mu^{(12)} = (1, \mathbf{0})$. $\rho_0^{(12)}$ represents the the total c.m. baryon density, which is not the sum of the rest densities $\rho_0^{(1)} + \rho_0^{(2)}$ of the currents but is larger because of Lorentz contraction. Therefore, in a naive LDA, Eqs. (8–10), the Lorentz contraction would be interpreted as a compression and could give misleading conclusions on the EOS. Thus a better approach in the LDA should be based on a total density given in terms of the rest densities.

The LCA should be able to adequately represent the time evolution of the phase space in a heavy ion reaction starting from the initial configuration of two separated cold Fermi ellipsoids, and ending up, possibly, with a thermalized fireball which corresponds to a single hot Fermi sphere. To give an impression on the quality of this representation we compare in Fig. 2 the LCA parametrisation to the phase space distribution obtained from the transport calculation, for a central ($b=0$) Au on Au reaction at 600 A.MeV for the NL2 parameter set. Here we show the local momentum space in the central region, i.e. around $\mathbf{x} = 0$, at three different time steps ($t=5, 25$ and 50 fm/c) which represent important stages of the reaction. The first configuration ($t=5$ fm/c) corresponds to the initial phase of the reaction where the nuclei start to overlap. The local momentum space still resembles the asymptotic initial configuration, i.e. it is given by two relatively sharp and well separated Fermi ellipsoids. In the compression phase ($t=25$ fm/c) where the density is maximal

a two-Fermi-ellipsoid configuration is still visible. However, the ellipsoids now strongly overlap and due to binary collisions their shapes become more and more diffuse. The expansion of the system leads to increasing equilibration and the momentum configuration finally evolves to one single Fermi sphere ($t=50$ fm/c). At this stage the LDA would be appropriate. In the right column of Fig. 2 a representation of the momentum distributions in the LCA are shown. The parameters of the configuration, i.e. the rest densities and the relative velocity of the currents are extracted from the phase space distribution of the transport calculation (left column) according to Eqs. (11–14). We then show in the right column of Fig. 2 a parametrization in terms of two Fermi-distributions of finite temperature with the given densities and relative velocity, taking also into account the Pauli-principle in the overlapping part. Details are given in ref. [12]. This shows that a more realistic description of the momentum configuration requires the inclusion of finite temperatures into the formalism, i.e. to replace sharp Fermi ellipsoids by diffuse covariant Fermi distributions. This is not done in the present implementation, but here sharp Fermi ellipsoids are used.

3.3 Self-energy

In the LCA the real part of the non-equilibrium self-energy Σ^+ is approximated by the self-energy in colliding nuclear matter with the corresponding parameters

$$Re\Sigma^+(x, p) = Re\Sigma^{(12)}(p_{F_1}(x), p_{F_2}(x), v_{rel}(x), p) \quad , \quad (16)$$

taken in the Hartree approximation. To evaluate the self-energies, Eqs. (16), they are expressed in terms of Lorentz invariants as for ground state nuclear matter [1,2,5]. These are naturally determined in the c.m. system. As in nuclear matter the self-energy can be decomposed into scalar and vector self energies

and the latter into time-like and space-like components [25,26]

$$\Sigma^{(12)\mu}(p) = \Sigma_0^{(12)} u^{(12)\mu} + \Sigma_v^{(12)}(p) \Delta^{(12)\mu\nu} p_\nu \quad (17)$$

with $\Delta^{(12)\mu\nu} = g^{\mu\nu} - u^{(12)\mu} u^{(12)\nu}$ the projector perpendicular on the total streaming velocity $u^{(12)}$. The invariant functions $\Sigma_{s,0,v}^{(12)}$ are obtained by covariant projections

$$\Sigma_s^{(12)} = \frac{1}{4} \text{tr}[\Sigma^{(12)}] \quad (18)$$

$$\Sigma_0^{(12)} = \frac{-1}{4} \text{tr}[u_\mu^{(12)} \gamma^\mu \Sigma^{(12)}] \quad (19)$$

$$\Sigma_v^{(12)} = \frac{-1}{4 (\Delta^{(12)\mu\nu} p_\mu p_\nu)} \text{tr} [\Delta^{(12)\mu\nu} p_\mu \gamma_\nu \Sigma^{(12)}] \quad . \quad (20)$$

To obtain the self-energies in a Hartree form, i.e. momentum independent, which is more convenient for the application in transport calculations, Eq. (7), these are averaged over the total momentum configuration [25]. In practice we restrict to symmetric systems, i.e. $p_{F_1} = p_{F_2}$, such that the $\Sigma_v^{(12)}$ vector part vanishes which simplifies the task considerably. The Hartree self-energy takes the form

$$\text{Re}\Sigma_H^{(12)} = \text{Re}\bar{\Sigma}_s^{(12)} - \gamma_\mu \text{Re}\bar{\Sigma}_0^{(12)} u^{(12)\mu} \quad , \quad (21)$$

where the averaged Lorentz invariants (18,19) are obtained as

$$\text{Re}\bar{\Sigma}_s^{(12)} = \int \frac{d^4p}{(2\pi)^4} \text{Re}\Sigma_s^{(12)}(p) \text{tr} [G^{<(12)}(p)] / \int \frac{d^4p}{(2\pi)^4} \text{tr} [G^{<(12)}(p)] \quad (22)$$

$$\text{Re}\bar{\Sigma}_0^{(12)} = \int \frac{d^4p}{(2\pi)^4} \text{Re}\Sigma_0^{(12)}(p) \text{tr} [u_\mu^{(12)} \gamma^\mu G^{<(12)}(p)] / \int \frac{d^4p}{(2\pi)^4} \text{tr} [u_\mu^{(12)} \gamma^\mu G^{<(12)}(p)] \quad (23)$$

As in [25] vertex functions are derived from the invariants in the following way

$$\bar{\Gamma}_s^{(12)} = -\frac{\text{Re}\bar{\Sigma}_s^{(12)}}{\rho_s^{(12)}} \quad , \quad \bar{\Gamma}_0^{(12)} = -\frac{\text{Re}\bar{\Sigma}_0^{(12)}}{\rho_0^{(12)}} \quad . \quad (24)$$

The Hartree self-energy in symmetric colliding nuclear matter is now given as

$$Re\Sigma_H^{(12)}(p_{F_i}, v_{rel}) = -\bar{\Gamma}_s^{(12)}(p_{F_i}, v_{rel})\rho_s^{(12)} + \gamma_\mu\bar{\Gamma}_0^{(12)}(p_{F_i}, v_{rel})j^{(12)\mu} \quad . \quad (25)$$

It is of the same structure as in the conventional $\sigma\omega$ -model [16], however the coupling constants for the scalar σ - and the vector ω -meson are replaced by vertex functions

$$\frac{g_\sigma^2}{m_\sigma^2} \mapsto \bar{\Gamma}_s^{(12)}(p_F, v_{rel}) \quad , \quad \frac{g_\omega^2}{m_\omega^2} \mapsto \bar{\Gamma}_0^{(12)}(p_F, v_{rel}) \quad , \quad (26)$$

which now contain the information on the anisotropy of the actual momentum space configuration.

In the Dirac-Brueckner approach the invariants, Eqs. (18-20), are given in terms of the T-matrix [1,2,5] and, in particular, in non-equilibrium by the respective non-equilibrium T-matrix. However, the T-matrix in colliding nuclear matter is not available at present. In [25] a procedure has been proposed to construct $\Sigma_{s,0,v}^{(12)}$ from a parametrisation of the ground state self energies and an extrapolation to the colliding nuclear matter system [25].

4 The effective fields

In the present work we compare mean fields derived from the microscopic Dirac-Brueckner approach to a phenomenological interaction, namely the non-linear $\sigma\omega$ -model. In Fig. 3 the equations-of-states, i.e. for ground state nuclear matter, are shown for the DB model [2] and a hard (NL3) and a soft (NL2) version of the non-linear $\sigma\omega$ -model [19]. The Dirac-Brueckner EOS is relatively soft and thus comparable to NL2 which is the reason why we mainly compare to this model. In Tab. 1 the corresponding nuclear matter bulk properties are shown: The saturation density, the binding energy, the compression modulus and the value of the effective mass m^* at saturation density. As discussed, e.g.,

in [54] the effective mass is a useful quantity to characterize the repulsiveness of the relativistic mean field which becomes less repulsive with increasing m^* . The DB model used here yields a small effective mass ($m^*/M = 0.586$). However, the explicit momentum dependence of the self energy also influences the behavior with density, such that the DB EOS is similar to the one of NL2 ($m^*/M = 0.83$).

In the following the DB model is applied in two approximations, in the Local Density Approximation (LDA) and in the Local Configuration Approximation (LCA) where the latter accounts for the non-equilibrium features of the process. The self-energy which enters into the transport equation (7) in both cases is used in the Hartree form given by Eq. (25). In the LDA the dynamical vertex functions $\Gamma_{s,0}(p_F)$ which parameterize the mean field depend only on the total density. Then the treatment is the same as in the case of finite nuclei [9,10] (however, rearrangement terms are not taken into account here.)

In the LCA the vertex functions depend on the subsystem densities of the nuclear matter currents and their relative velocity v_{rel} (14). In the present calculations we have restricted the determination of the colliding nuclear matter mean fields to symmetric systems, i.e. $p_{F_1} = p_{F_2}$ which we take as the mean value of the subsystem densities. The dynamical vertex functions $\bar{\Gamma}_{s,0}^{(12)}$ for colliding nuclear matter are determined as described in Ref. [25]. Thus, they include exchange and correlations effects of the in-medium T-matrix and therefore the most relevant dynamical effects of the non-equilibrium phase space. Of course, the approach of [25] only approximates the solution of the full problem, i.e. the solution of the Bethe-Salpeter equation for arbitrary anisotropic configurations. The approach neglects the non-equilibrium effects originating from the configuration dependence of the Pauli operator in the intermediate states of the Bethe-Salpeter equation, which should, in principle, be evaluated for two-Fermi-ellipsoid configurations [56].

For practical purpose the vertex functions determined as in Ref. [25] are parametrised in the following way

$$\bar{\Gamma}_{s,0}^{(12)}(\rho_0^{(i)}, v_{\text{rel}}) = \alpha_{s,0} e^{-\beta_{s,0}(\rho_0^{(1)} + \rho_0^{(2)})} + \gamma_{s,0} \quad . \quad (27)$$

This allows an extrapolation to small densities ($\leq 0.5\rho_{\text{sat}}$) where no DB self-energies have originally been available [2] for the construction discussed above. In table 2 the coefficients α , β and γ , Eq. (27), are given for different streaming velocities v in the c.m. system of the currents. In symmetric systems these are $u_{\mu}^{(1)} = (\gamma, \gamma v)$ and $u_{\mu}^{(2)} = (\gamma, -\gamma v)$ with the relative velocity $v_{\text{rel}} = \frac{2v}{1+v^2}$. In Fig. 4 the $\bar{\Gamma}_{s,0}^{(12)}$ are shown in dimensionless units as functions of the subsystem densities $\rho_0^{(i)}$ and the c.m. streaming velocities v . The overall behavior of the scalar and vector vertex functions is quite similar. Both generally decrease with increasing density, however, the momentum or velocity dependence is more complex [25]. It should be kept in mind that the non-relativistic mean field involves a cancellation of the scalar and vector self-energies (see Eq. (28), below) and thus reacts sensitively to small variations of these functions. The corresponding coupling constants of the $\sigma\omega$ -model (QHD1) [16] are $\frac{g_{\sigma}^2}{m_{\sigma}^2} \frac{M^2}{4\pi} = 21.25$ and $\frac{g_{\omega}^2}{m_{\omega}^2} \frac{M^2}{4\pi} = 15.95$.

The vertex functions, Eq. (27), and the self-energy, Eq. (25) are now used to approximate the non-equilibrium self-energy Σ_H^{\pm} in the kinetic equation (7) in the spirit of the LCA, i.e. by extracting locally the parameters $p_{F_i}(x)$ and $v_{\text{rel}}(x)$. In the local density approximation (DB/LDA) these coupling functions are used at zero relative velocity and at the total density $\bar{\Gamma}_{s,0}^{(12)}(\rho = \rho_0^{(1)} + \rho_0^{(2)}, v_{\text{rel}} = 0)$.

A useful quantity to characterize the mean field is the real part of the optical potential. The nucleon-nucleus optical potential is well known from proton scattering data [47] and has been used to fit the momentum dependence of mean fields [29,30]. The quantity of interest in a heavy ion collision is the

nucleon optical potential in a nucleus–nucleus collision. In colliding nuclear matter it is obtained as [25]

$$ReU_{\text{opt}}(E) = Re\bar{\Sigma}_s^{(12)} - \left(\frac{E}{M} + 1\right) Re\bar{\Sigma}_0^{(12)} + \frac{(Re\bar{\Sigma}_s^{(12)})^2 - (Re\bar{\Sigma}_0^{(12)})^2}{2M} \quad (28)$$

with E the mean incident energy of a nucleon in the colliding system. It depends on the incident energy E also through the relative velocity v_{rel} in the self-energies in Eq. (16). A corresponding potential in the LDA is the nucleon optical potential of a nucleon of energy E in nuclear matter. It is given also by expression (28) which $\Sigma^{(12)}$ replaced by the equilibrium nuclear matter self-energies taken at the total density $\rho_B = \rho_0^{(1)} + \rho_0^{(2)}$. Thus, referring back to Fig. 1, the nucleon–nucleus potential is experienced by a nucleon in the left configuration, i.e. a distance P_{inc} away from the center, while the potential in the nucleus–nucleus collision is the potential experienced by a nucleon in the mean in the right two–ellipsoid configuration.

These optical potentials are compared in Fig. 5. The DB nucleon–nucleus optical potential [2] at saturation density and two times saturation density is compared to the optical potential of a mean nucleon in a nucleus–nucleus collision. As can be seen the overall behavior of the different potentials is similar, in that the behavior with increasing energy is dominated by the repulsive vector fields. However, the nucleus–nucleus optical potential in general is less repulsive. This effect increases in significance with increasing density and is quite distinct at $2\rho_{\text{sat}}$, a density which is easily reached in a heavy ion collision. On the average the nucleon in the two-stream configuration sees lower momentum components than in the one–sphere configuration.

Fig. 5 also shows the experimental data [47] which should be compared to the nucleon–nucleus potential. It is seen that the DB results of ter Haar and Malfliet [2] used in the present work are in a reasonable agreement with the data below 1 GeV incident energy. We mention that in Ref. [5] very similar

results have been obtained for the real part of the optical potential by relativistic Brueckner calculations using the Bonn potentials. Generally, all these calculations start to overshoot the optical potential at energies above 1 GeV. This deviation from the empirical values may be due to the fact that the underlying NN interaction, i.e. the one-boson-exchange potentials, [2,7] are fitted to low energy phase shifts up to 300 MeV. Furthermore, with increasing energy the excitation of baryonic resonances which is not included in standard Brueckner calculations, may start to play an important role and also particle production starts to influence the reaction dynamics. The NL2 parameterization of the $\sigma\omega$ -model considerably underestimates the data in the energy range considered.

5 Numerical realization

5.1 The relativistic Landau-Vlasov method

In this section we discuss questions related to the numerical simulation of the relativistic BUU equation. As in other works we adopt a test particle method, however, we use covariant extended test particles of Gaussian shape in coordinate and momentum rather than point-like test particles [19,55]. This method was called 'relativistic Landau-Vlasov' method and is extensively discussed in Ref. [21]. Here we only recall the main features of this approach.

The $8 \cdot (N \cdot A)$ -dimensional phase space distribution of the testparticles is given as

$$\begin{aligned} (aF)(x, p^*) &= \frac{C}{N} \sum_{i=1}^{A \cdot N} \int_{-\infty}^{\infty} d\tau g(x - x_i(\tau)) \tilde{g}(p^* - p_i^*(\tau)) \\ &= \frac{C}{N (\pi \sigma \sigma_p)^3} \sum_{i=1}^{A \cdot N} \int_{-\infty}^{\infty} d\tau e^{(x-x_i(\tau))^2/\sigma^2} e^{(p^*-p_i^*(\tau))^2/\sigma_p^2} \end{aligned}$$

$$\times \delta [(x_\mu - x_{i\mu}(\tau)) u_i^\mu(\tau)] \delta [p_\mu^* p_i^{*\mu}(\tau) - m_i^{*2}] \quad . \quad (29)$$

Here N is the number of test particles per baryon and the factor $C = \frac{1}{4}(2\pi)^4$ normalizes the phase space. g and \tilde{g} are the gaussian shapes of the test particles in coordinate and momentum space, and (x_i, p_i) are the centers of the test particles. The δ -function constraints in Eq. (29) serve to fix the eigentime τ on the world line, to reduce the phase space to $7 \cdot (N \cdot A)$ dimensions, and to ensure the arguments of the exponentials to be purely space-like. The centers of the gaussians are put on the mass-shell $p_i^{*2} = m_i^{*2}$. In general the momentum space gaussians lead to off-shell contributions and thus include a model for the spectral function in a simple way. As shown in Ref. [21] the width of the momentum space gaussian is related to the spectral width and hence should evolve dynamically. In the present calculations these widths are, however, kept constant. For this work the advantage of the use of gaussians lies in a smoother representation of the phase space.

Performing a p_0 -integration the seven-dimensional distribution is obtained as

$$\begin{aligned} F(x, \mathbf{p}^*) &= \int \frac{dp_0}{2\pi} (aF)(x, p^*) \\ &= \frac{C}{N2\pi} \sum_{i=1}^{A \cdot N} \int_{-\infty}^{\infty} d\tau g(x - x_i(\tau)) \frac{1}{p_{i0}^*} e^{\left(\frac{\mathbf{p}_i^{*2}}{p_{i0}^{*2}} - (\mathbf{p}^* - \mathbf{p}_i^*)^2\right) / \sigma_p^2} \quad . \quad (30) \end{aligned}$$

We also note that this ansatz is consistent with the sum rule for the spectral function [23]. To evaluate the gaussians in Minkowski space the τ -integration over the world line of the particle is carried out by expanding the trajectory locally into a Taylor series up to first order around an eigentime $\hat{\tau}$ which is fixed by the condition $x_0 = x_{i0}(\hat{\tau})$. Then the gaussian in Minkowski space reduces to

$$\int_{-\infty}^{\infty} d\tau g(x - x_i(\tau)) = (\sqrt{\pi}\sigma)^{-3} e^{R_{i\mu}(x)R_i^\mu(x)/\sigma^2} \quad (31)$$

with $R_i^\mu(x) = (x^\mu - x_i^\mu(\hat{\tau})) - (x_\nu - x_{i\nu}(\hat{\tau})) u_i^\nu(\hat{\tau}) u_i^\mu(\hat{\tau})$ which is the distance

in Minkowski space perpendicular to the four-velocity $u_i(\hat{\tau})$ of the particle.

The phase space distribution, Eq. (29), provides a solution of the Vlasov equation, i.e. the drift term of the kinetic equation (7), if the testparticles obey classical equations of motion [21]

$$\begin{aligned}\frac{dx_i^\mu}{d\tau} &= \frac{p_i^{*\mu}(\tau)}{m_i^*(x_i)} \\ \frac{dp_i^{*\mu}}{d\tau} &= \frac{p_{i\nu}^*(\tau)}{m_i^*(x_i)} F^{\mu\nu}(x_i(\tau)) + \partial^\mu m_i^*(x_i) \quad .\end{aligned}\tag{32}$$

The DB mean fields in LCA and LDA are determined in every time step as described in the previous section. For the simulation of the collision term we adopt the full ensemble method [15] and use the Cugnon parametrisation of the NN cross section [52]. In the considered energy range inelastic channels already play an important role [55], in particular the $\Delta(1235)$ -resonance influences the dynamics to a large extent. The production and the decay of Δ -resonances as well as pion production and reabsorption are included as described in Ref. [57]. The initialization of the nuclei is performed as described in Ref. [21].

5.2 Fragment content in RLV

The RLV method is a successful tool to simulate heavy ion reactions in the framework of relativistic transport theory. It accurately reproduces the one-body dynamics of the colliding system [55] and thus yields reliable results of global flow observables. This will be discussed in section 6. One-body models, however, do not contain dynamical fluctuations which become significant in instability situations in the decompression stage of the reaction, and which are important for the formation of fragments. The theoretical description of higher order correlations and hence of dynamical fragment formation is actively debated, and there have been various attempts to describe the higher order correlations approximately: by adding a fluctuation term leading to the

Boltzmann Langevin equation [58], by choosing the numerical fluctuations in a judicious way by the number of test particles [59], or by introducing fluctuations directly into the phase space distribution [60].

In this work we will not address this question. However, we need information about the fragmentation in the final state of the reaction in order to perform a reliable comparison with experiments which are sensitive to the fragments via detector acceptances. Therefore, we will restrict ourselves to a simple model which generates intermediate mass fragments. We then adopt the FOPI filter simulation (see next section) which depends on the fragment charge.

A simple way to generate fragments from the final phase space is the phase space coalescence model [61,62]. It is a method to generate many-body correlations which are consistent with a given one-body distribution function. Within this model a number of nucleons form a fragment if their distances in coordinate as well as in momentum space are smaller than certain coalescence parameters R_c and P_c , respectively

$$|\vec{x}_i - \vec{X}_f| \leq R_c \quad , \quad |\vec{p}_i - \vec{P}_f| \leq P_c \quad .$$

Here \vec{x}_i and \vec{p}_i are the coordinates of the i -th nucleon in coordinate and momentum space, respectively, and \vec{X}_f and \vec{P}_f are the center-of-mass coordinates of the fragment. From the distribution of the $N \cdot A$ test particles of a simulation, A test particles are chosen at random and the above procedure is applied at the final time step of the calculation. This generates a fragmentation "event", and to generate distributions this procedure is repeated many times (≈ 10000). Thus the fragment formation is modeled by the choice of the parameters R_c and P_c which are effective parameters. They are determined by a fit to the experimental charge distributions. This procedure has to be carried out for each interaction separately.

In order to give an impression of this procedure we show in Fig. 6 the charge

distributions obtained for two different mean fields, the non-equilibrium DB forces (DB/LCA) and the non-linear $\sigma\omega$ model NL2. As an example we use central and peripheral Au on Au reactions at different incident energies. The experimental curves are taken from FOPI [27] and represent 4π charge distributions extrapolated within the blast model [63]. The coalescence parameters have been adjusted such that both theoretical distributions yield similar abundances of light fragments ($Z \leq 3$). However, the DB model in LCA (and in LDA not shown here) produces too many heavy fragments ($Z \geq 3$). This is also evident from test particle distributions (not shown here), which are considerably more "lumpy" than for NL2. The reason may be due to the extrapolation of the DB nuclear matter results to densities below half saturation density (see the discussion in section 4). In any case, deviations for higher Z between the experimental and theoretical distributions will have no consequence in the following flow analysis, since the absolute yields of heavy fragments ($Z \geq 3$) is exponentially decreasing and multiplicity distributions and flow observables are governed by the dynamics of protons and light fragments. The fit procedure, which has been performed in the energy range from 250 to 800 A.MeV, ensures a correct inclusion of detector acceptance cuts simulated by the filter program. The coalescence parameters $R_c \sim 4 \text{ fm}$ and $P_c \simeq 1.4 \text{ fm}^{-1}$ are similar to values obtained from QMD simulations [29].

6 Flow analysis

We now study the global flow observables and compare them to experiments, in particular we discuss recent flow data measured by the FOPI collaboration [42–45,64,65]. These flow data were obtained with the Phase I of the FOPI detector at the SIS/ESR accelerator facility at the GSI. For details we refer to work of the FOPI collaboration [31,42,43] and references therein. Relative to earlier experimental investigations [46] these new experiments have the

advantage of high selectivity concerning the detection of intermediate mass ($Z \geq 3$) fragments up to $Z = 15$. This ability of the FOPI detector allows a cleaner identification of the collective flow signal and thus provides flow data of high precision for different fragments over an energy range of several hundred A.MeV. A wide range of the impact parameters has been explored which offers the possibility to study the centrality dependence of the observables. We discuss flow observables concerning the reaction dynamics in the reaction plane (in-plane flow) and perpendicular to the reaction plane (out-of-plane flow).

A reliable comparison to the data requires to account for the detector acceptances, such as geometrical cuts and thresholds, which is achieved by the FOPI filter simulation code [66]. Fragments are generated as outlined above. Furthermore, the correspondence between the centrality classes of the reaction (impact parameters) and the multiplicities of the detected charged particles (PM) (see next section) has to be determined. In the following analysis we choose the z -axis as the beam direction, and the reaction plane as the xz -plane, where the projectile and target are asymptotically shifted by the impact parameter b in the x -direction.

6.1 Centrality selection

A problem in any experimental analysis is that it does not allow a direct determination of the impact parameter of the reaction. The usual procedure is to extract the centrality of the reaction from the measurement of strongly impact parameter dependent observables. The correlation between these quantities and an impact parameter range or centrality class has to be obtained in a model. In the FOPI experiments several observables have been investigated

to select the centrality class of the reaction [27,31,42]. One is the *ERAT*-ratio

$$ERAT = \left(\sum_{i=1} \frac{E_{\perp}^{(i)}}{E_{\parallel}^{(i)}} \right)_{Y^{(i)} \geq Y_{c.m.}} \quad (33)$$

defined by the ratio of the transverse E_{\perp} and the longitudinal kinetic energy E_{\parallel} . The sum in Eq. (33) runs over all nucleons in the forward hemisphere, characterized by $Y^{(i)} \geq Y_{c.m.}$ ($Y^{(i)}$ being the rapidity of particle i). Thus the *ERAT* value is a measure of the amount of the kinetic energy transferred perpendicular to the beam axis. The pronounced impact parameter dependence is illustrated in Fig. 7 where the *ERAT* ratio at different energies is shown as a function of the impact parameter. Large (small) values of *ERAT* correspond to central (peripheral) reactions. Due to the strong variation at small values of b the *ERAT* observable is particularly suited for the selection of very central reactions [27]. In our previous comparison [11] to flow data [31] the *ERAT* distributions has been used to select the centrality classes of the reactions. A detailed discussion of the *ERAT* selection can be found in the work of Reisdorf et al. [27].

Another suitable observable to determine the centrality class of the reaction is the charged particle multiplicity PM . This observable measures the number of detected particles with charge $Z \geq 1$ from the participant matter. Thus, high (low) multiplicity values correspond to central (peripheral) reactions. Such multiplicity distributions show a typical plateau for small PM -values and a strong decrease with increasing multiplicity [27]. Thus they are sensitive to peripheral collisions. The multiplicity bins which correspond to different centrality classes, are usually defined in the following way: the lower limit of the highest multiplicity bin $PM5$ is fixed at half of the plateau value, and the remaining multiplicity range is divided into four equally spaced intervals, denoted by $PM4$ to $PM1$. $PM5$ then corresponds to most central reactions [27,42–45].

The theoretical charge distributions (see Fig. 6) and the corresponding multiplicity distributions are model dependent. Hence, the correlation between the charged-particle multiplicity PM and the centrality class has to be established separately for each model and for different energies. Table 3 gives for the different models the lower limits PM_L for the highest multiplicity bin PM_5 . The corresponding experimental values are taken from Ref. [43]. The theoretical determination of the impact parameter range $[b, b + \Delta b]$ follows from the calibration curves PM versus b . Fig. 8 shows this correlation between the PM multiplicity and the impact parameter b for two of the mean fields applied. Both curves show the typical decrease of PM with increasing impact parameter. However, the absolute PM values differ due to different charge distributions (see Fig. 6). As discussed above, the DB/LCA approach, and very similarly also DB/LDA (not shown here), yield more heavy clusters and therefore a smaller total yield of charged particles than NL2. The centrality calibration used here takes such facts into account and provides the correct correlation between the impact parameter range and the multiplicity bins for each model. In table 4 mean impact parameters

$$\langle b \rangle = \frac{\int_{b_{\min}}^{b_{\max}} b \cdot b db}{\int_{b_{\min}}^{b_{\max}} b db} = \frac{2 (b_{\max}^3 - b_{\min}^3)}{3 (b_{\max}^2 - b_{\min}^2)}$$

are given for the system Au on Au at the various energies considered.

6.2 In-plane flow

An important observable to characterize the dynamical evolution of the reaction is the mean transverse momentum projected on the reaction plane $\langle p_x(Y_{c.m.}) \rangle$ as a function of the center-of-mass rapidity $Y_{c.m.}$, often also denoted as "bounce-off", "transverse flow" or "sideward flow". It is sensitive essentially only to the mean field, in particular on its repulsiveness, and has thus been regarded as a source of information on the nuclear EOS [19,67]. For

a first discussion we compare in Fig. 9 the sideward flow per nucleon as a function of the normalized rapidity $Y^{(0)} = Y_{\text{c.m.}}/Y_{\text{proj}}$ obtained with the DB/LCA and NL2 models in a semi-central Au on Au reaction at 600 A.MeV. In a comparison to experiment one has to take into account the influence of the acceptance filter on the in-plane flow. In previous works [27,31,42–44] mainly in the non-relativistic QMD model it was found that the FOPI filter scarcely affects the shape of the in-plane flow in the forward hemisphere ($Y^{(0)} \geq 0$). This is confirmed in the present calculations, Fig. 9, where the filtered as well as the unfiltered in-plane flow is shown. Therefore this observable can reliably be compared to the data.

The results of Fig. 9 also show the strongly repulsive character of the DB/LCA mean fields relative to NL2. We note that the repulsion in relativistic transport models originates mainly from the momentum dependence, in contrast to non-relativistic approaches as BUU [15] or QMD [29] where the density dependence is decisive. Although both models, DB and NL2, yield a similar density dependence, i.e. comparable slopes of the EOS at high densities, as seen in Fig. 3, the reaction dynamics is very different in the two cases. Thus the sideward flow generated by the repulsive momentum dependent part of the field is different in the two models as already seen in the optical potentials of Fig. 5. A scaling behavior of the in-plane flow with the inverse of the value of m^* has, e.g., been discussed in Ref. [54].

We have analyzed the sideward flow with respect to centrality and fragment charge, as in the experimental data. We start the discussion with the sideward flow of protons ($Z = 1$) shown in Fig. 10. The theoretical results are compared to the FOPI data for the system Au on Au at incident energies of 250, 400 and 600 A.MeV and for two typical centrality classes, i.e. *PM5* (central collisions) and *PM4* (semi-central reactions). For the relation between the impact parameter ranges and the multiplicity bins we refer to table 4. We find that the DB/LCA mean fields are generally able to reproduce the sideward flow of

protons over the considered energy range. In particular, for the most central (*PM5*) reactions the agreement between the DB/LCA results and the data is excellent for the range $0 \leq Y^{(0)} \leq 1.2$. At higher rapidities slight deviations occur which, however, could also be due to statistical fluctuations. Comparing to the local density approximation DB/LDA we see that non-equilibrium effects are most pronounced in central collisions (*PM5*). Here DB/LDA yields generally a larger flow and strongly overestimates the data. With increasing impact parameter the description with DB/LCA becomes less accurate and slightly overestimates the data. This behavior was already observed in Ref. [11]. This may be due to a simplification in our treatment in that the non-equilibrium mean fields are always determined for symmetric configurations [25], i.e. the local 2-Fermi-sphere momentum configurations are symmetrized at $p_{F_1} = p_{F_2}$. Such a treatment should be better in central collisions which exhibit a high symmetry of the local phase space. In more peripheral collisions, however, asymmetric configurations where the densities of projectile and target are significantly different become more important and the approximation is less accurate.

The $\sigma\omega$ mean field (NL2), on the other hand, leads to substantial underestimation of the in-plane flow for all incident energies and centrality classes. Obviously the momentum dependent repulsion is too small in this model.

In Figs. 11, 12 and 13 the in-plane flow per nucleon $\langle p_x/A \rangle$ for light fragments with charges $Z = 2, 3$ and 4, respectively, is shown at incident energies of 250, 400 and 600 A.MeV and for the same centrality classes as in Fig. 10. First of all, it is seen that all models are able to qualitatively reproduce the increasing in-plane flow per nucleon with increasing fragments size. The enhanced flow most likely results from the fact that these large fragments are created in the cool spectator regions. In Ref. [12] it was also found that thermodynamical instabilities appear after the compression phase in the cool spectator regions. Such a scenario is also supported by QMD calculations where it is found that

heavy fragments show a smaller stopping than protons [68]. The dependence of the fragment flow on the mean field model is again pronounced. As in the case of protons the DB model generally yields a higher in-plane flow than NL2. The importance of non-equilibrium effects seems to decrease with increasing fragment size. E.g. for $Z=4$ there are no significant differences visible between DB/LCA and DB/LDA whereas for $Z=2$ the situation is still similar to the case of $Z=1$. However, the comparison of the different calculations with the data is not so conclusive. For peripheral reactions ($PM4$) the DB/LCA approach is able to reproduce better the fragment dynamics whereas NL2 again underestimates the data for rapidities greater than ~ 0.5 . However, for central reactions ($PM5$) the opposite trend is observed, i.e. the DB calculations overestimate the data whereas NL2 only slightly underestimates them. Thus, a reliable comparison to dynamical observables derived from fragment distributions seems problematic. Theoretical predictions could be strongly influenced by the models of fragment formation and a simple phase space coalescence model could be insufficient in order to draw reliable conclusions. Such problems are perhaps smaller when integrated observables are considered, which we do now.

The mean directed in-plane flow per particle P_x^{dir}/A in one event is defined as

$$P_x^{\text{dir}}/A = \frac{\sum_{i=1}^M p_x^{(i)} \text{sign}(Y_i^{(0)})}{\sum_{i=1}^M A_i} \quad (34)$$

where the sum in Eq. (34) runs over all M fragments of an event in a given centrality class and A_i and $p_x^{(i)}$ is the mass number and transverse momentum of the i -th particle, respectively. P_x^{dir} is a very useful observable to classify the global reaction dynamics, because, except for detector cuts, it is independent of the fragment generation procedure. Fig. 14 shows the energy dependence of $\langle P_x^{\text{dir}}/A \rangle$, i.e. averaged over many events. It is seen that the non-equilibrium DB mean fields are able to reproduce the correct energy dependence of the directed in-plane flow over the energy range from 250 up to 600 A.MeV. At

800 A.MeV it slightly overestimates the data, however, at this energy the DB approach [2,5] also starts to overestimate the empirical optical potential (real part). Neglecting non-equilibrium effects (DB/LDA) generally leads to a larger flow. The relative importance of these effects is small at 250 A.MeV, maximal at 400 A.MeV and then decreases again with increasing energy. This energy dependence is reasonable since at 250 A.MeV the initial relative velocity of the local nuclear matter currents, i.e. the anisotropy of the phase space, is still small and at high energies elastic and inelastic NN-scattering processes start to dominate the reaction dynamics. Interestingly, the mean field effects are most pronounced at 400 A.MeV where the sideward flow excitation function, i.e. the flow scaled by the beam energy, is maximal as well [69].

Fig. 15 illustrates the centrality dependence of P_x^{dir} at 400 and 600 A.MeV. The dependence of P_x^{dir} on the impact parameter shown in the left panels does not depend strongly on the energy in the two cases. The in-plane flow is maximal at impact parameters between 4–5 fm. It rapidly drops down to zero with decreasing impact parameter which reflects the symmetry around the beam axis in very central collisions. The DB/LCA mean field yields a maximum value of P_x^{dir} which is about twice as large as that reached with the softer NL2 model, which was already seen in Fig. 10. Applying the local density approximation DB/LDA the flow signal is again increased by about 30% compared to DB/LCA. As already seen in the previous figure this effect is maximal at 400 A.MeV. In the right panels of Fig. 15 the directed flow as a function of the centrality class determined with the multiplicity selection is compared to the data [64]. The PM dependence of P_x^{dir} is obtained by averaging $P_x^{\text{dir}}(b)$ over the corresponding PM classes given in Tab. 4

$$\langle P_x^{\text{dir}}(PM) \rangle = \frac{\int_{b_{\min}}^{b_{\max}} P_x^{\text{dir}} b^2 db}{\int_{b_{\min}}^{b_{\max}} b^2 db} . \quad (35)$$

In this context it should be noticed that the PM selection is less accurate for very central collisions. At small impact parameters the multiplicities almost

saturate, see Fig. 8, which leads to an insufficient b resolution below $b \leq 2 - 3$ fm. Consequently, the measured $P_x^{\text{dir}}(PM)$ is actually not zero for the highest multiplicity, but corresponds to central reactions at $b \sim 3$ fm [27,43,45]. A better resolution of very central events can be achieved by the ERAT selection, see Fig. 7. This problem was extensively discussed in Ref. [27]. The comparison to the data in Fig. 15 clearly shows that the DB/LCA calculations are able to reproduce the in-plane flow for central up to semi-central reactions. Here the local density approximation DB/LDA again leads to a strong overestimation of the data. Only in peripheral collisions corresponding to low multiplicities, $PM/PM_{5L} \sim 0.4$, the local density approximation is reliable.

6.3 Out-of-plane flow

The emission of nuclear matter perpendicular to the reaction plane, the so-called "squeeze-out", is another characteristic feature of heavy ion collisions. This effect is mainly caused by the fireball expansion and the shadowing by spectator matter in the reaction plane. The out-of-plane emission is therefore most pronounced close to the mid-rapidity region. It was predicted by early hydrodynamical calculations [70,71] and later confirmed experimentally [72,73]. Since the out-of-plane emission mainly originates from the participant region it contains direct information on the highly compressed nuclear matter and is sensitive on the nuclear EOS [74,75].

Before analyzing the squeeze-out in detail it is helpful to investigate its formation, i.e. the transition from the in-plane to the out-of-plane flow. Azimuthal distributions around the beam direction $dN/d\Phi$ (where Φ is the azimuth of the particles with respect to the reaction plane) with changing center-of-mass polar angle $\Theta_{\text{c.m.}}$ are suitable to study the formation of squeeze-out [44]. Fig. 16 compares azimuthal emission patterns at different polar angles for a semi-central ($PM4$) Au on Au reaction at 600 A.MeV to the FOPI data [44].

At forward polar angles the distributions exhibit strongly enhanced in-plane emission along the sideward flow direction of the projectile ($\Phi = 0^\circ$ and 360°). Increasing $\Theta_{\text{c.m.}}$ a sudden change in the azimuthal emission pattern is observed for $\Theta_{\text{c.m.}} \geq 70^\circ$. At $\Theta_{\text{c.m.}} \approx 90^\circ$ the azimuthal distributions clearly show maxima at $\Phi = 90^\circ$ and $\Phi = 270^\circ$ which are evidence for the squeeze-out. Both models, DB/LCA and NL2, are in qualitative agreement with the data, for NL2 it is almost quantitative. This indicates that the dynamical evolution of the out-of-plane emission is correctly described by these forces. On the other hand, DB/LDA leads to an extremely strong squeeze-out signal for large polar angles approaching $\Theta_{\text{c.m.}} = 90^\circ$. The particles around $\Theta_{\text{c.m.}} = 90^\circ$ preferentially belong to the stopped fireball matter and the strong repulsion of the DB/LDA force seems to push out these particles too rapidly from the fireball region resulting in a too large squeeze-out.

As a quantitative measure of this transition from in-plane to out-of-plane flow the anisotropy ratio R has been proposed [44]

$$R = \frac{dN/d\Phi \big|_{0^\circ < \Phi < 45^\circ} + dN/d\Phi \big|_{315^\circ < \Phi < 360^\circ}}{dN/d\Phi \big|_{135^\circ < \Phi < 225^\circ}} \quad , \quad (36)$$

considered as a function of $\Theta_{\text{c.m.}}$. It was found that at intermediate polar angles the FOPI filter scarcely affects the anisotropy ratio R and a reliable comparison to the data [44] can be performed. This is done in the Fig. 17. It is seen that the DB mean fields yield a significantly higher anisotropy than the NL2 model and strongly overestimate the data at intermediate and larger polar angles. Since the squeeze-out effect which is maximal at $\Phi = 90^\circ, 270^\circ$ degree, is not covered by the ratio defined in Eq. (36) DB/LCA and DB/LDA yields similar results for R although they have completely different out-of-plane emission patterns. The NL2 model leads to a much smoother $\Theta_{\text{c.m.}}$ -dependence of R but generally underestimates the data. Comparing with QMD calculations [44] it seems that the momentum dependence of the DB mean forces is responsible for the overestimation of R . Momentum dependent Skyrme forces (hard and

soft) yield qualitatively similar results as DB whereas a static hard Skyrme force gives results closer to the data and more comparable to NL2. On the other hand, the momentum dependence in the last section was found to be essential for the correct in-plane dynamics which is reflected in Fig. 17 by the observation that the DB/LCA calculation is closer to the data at forward angles. This indicates that the strong repulsion provided by the DB model yields a reasonable description of the in-plane dynamics of the spectator matter but the model has problems to describe exactly the flow evolution of the stopped matter in the fireball region. Thus, additional effects as in-medium modifications of the NN cross section [26,34,36] may play a role. However, non-equilibrium effects (DB/LCA) again turn out to be essential and improve the agreement with the experimental observations.

We now discuss the out-of-plane emission of participant matter at mid-rapidity, i.e. $-0.15 \leq Y^{(0)} \leq 0.15$ where the squeeze-out signal is maximal [42,43,45,65,64]. To take the limited detector acceptance into account means to make cuts with respect to the normalized transverse momentum per nucleon $P_T^{(0)} = \frac{(P_T/A)}{(P_T^{\text{proj}}/A_p)}$ [42,43,45]. Fig. 18 shows the influence of the FOPI filter on the squeeze-out, for NL2 as an example. The calculations are performed with and without the FOPI filter and a $P_T^{(0)}$ -cut ($0.06 \leq P_T^{(0)} \leq 0.55$), respectively. The solid lines are fits to the theoretical distributions according to

$$N(\phi) = \alpha_0 (1 + \alpha_1 \cos(\phi) + \alpha_2 \cos(2\phi)) \quad . \quad (37)$$

From Eq. (37) a quantity called the squeeze-out ratio is obtained as

$$R_N = \frac{1 - \alpha_2}{1 + \alpha_2} \quad . \quad (38)$$

If the $P_T^{(0)}$ cuts are taken into account the filter has only a small influence within the statistical uncertainties ($R_N = 1.226 \pm 0.04$ without filter and cuts and $R_N = 1.15 \pm 0.03, 1.168 \pm 0.03$ with $P_T^{(0)}$ -cut but without and with filter,

respectively). A similar observation was made in Ref. [42].

In Fig. 19 the model dependence of the squeeze-out signal is considered, i.e. the results for the DB forces DB/LCA and DB/LDA and the NL2 are compared. The calculations are performed for a semi-central (PM4) Au on Au reaction at 600 A.MeV and the FOPI filter has been applied. As already observed in Fig. 17 we see a strong dependence of the out-of-plane flow on non-equilibrium effects. The local density approach to the DB mean field (DB/LDA) leads to a much stronger out-of-plane flow compared to the case when non-equilibrium effects are taken into account (DB/LCA). On the other hand, DB/LCA still gives a stronger signal than the softer NL2 model. Thus the out-of-plane flow shows the same general dependence on the nuclear mean field as the in-plane-flow. In the upper panel of Fig. 19 we compare the NL2 result to the corresponding FOPI data [45] for both, $Z = 1$ and $Z = 2$. The theoretical curve somewhat overestimated the squeeze-out signal for $Z = 1$ but is in agreement with the $Z = 2$ data. Since the experimental results are partially biased by detector inefficiencies [45] but exhibit a strong charge dependence it seems to be more reasonable to compare in average to the $Z = 1$ and $Z = 2$ data. Doing this, NL2 and also DB/LCA slightly overestimate the data but are in qualitative agreement whereas DB/LDA strongly overpredicts the out-of-plane emission.

Selecting particles with high transverse momentum an even more pronounced dependence on the EOS has been observed [45]. Thus, in the following we concentrate on the analysis of high $P_T^{(0)}$ -particles, which are selected by a cut $0.5 \leq P_T^{(0)} \leq 0.55$. Fig. 20 shows the corresponding R_N ratio Eq. (38) in semi-central reactions (PM4) as a function of the incident energy. Here the results for DB/LDA are not shown since they have already been shown to be completely off the data. For the high energetic particles NL2 again underestimates whereas DB/LCA tends to overestimate the data. Only at the highest energy considered, i.e. at 800 A.MeV, the calculations agree with the exper-

iment. Except for the lowest data point both models miss the experimental curve equally, however, due to the narrow energy window the statistical errors of the calculations are rather large, in particular at 250 A.MeV.

Both models, DB and NL2, do not provide a quantitative description of the out-of-plane dynamics. The DB forces generally yield larger squeeze-out and anisotropy ratios which is consistent with the in-plane analysis and can be explained with the repulsive character of the nuclear fields. It is clear, however, that the inclusion of non-equilibrium effects is essential for a reasonable description of the reaction dynamics. In-medium modifications of the NN cross section may further influence the azimuthal distributions since the shadowing effects by the spectator matter are strongly governed by binary collisions.

7 Summary and conclusions

We studied the reaction dynamics in intermediate energy heavy ion collisions in the framework of relativistic transport theory and compared collective in-plane and out-of-plane flow observables to experimental data obtained by the FOPI Collaboration. In order to obtain a more complete picture these investigations covered a wide range of incident energies (250 to 800 A.MeV) and the full centrality range ($0 \leq b[fm] \leq 14$). The limitations of detector acceptances were taken into account by generating fragment distributions by a coalescence model.

The nuclear mean field used in the transport calculations was based on relativistic Dirac-Brueckner (DB) theory. We argue that the colliding system is far away from global and even local equilibrium during most of the reaction and therefore a local density approximation (LDA) of the mean field may not be justified. Thus we account for the non-equilibrium features of the dynamical phase space configuration also on the level of the mean field. The mean

field is parameterized for a class of anisotropic phase space configurations given by 2-Fermi-ellipsoid configurations in momentum space. We called this approximation "local (phase space) configuration approximation (LCA)" in contrast to the commonly used local density approximation (LDA). We further compared this microscopic approach to a non-linear parameterization of the $\sigma\omega$ model (NL2) which provides similar density dependence, i.e. a similar nuclear matter equation-of-state, as the DB model, however, a significantly less repulsive optical potential.

The analysis of in-plane flow observables demonstrates that the DB mean fields are generally able to provide a reliable description of the reaction dynamics. However, the inclusion of non-equilibrium features in the interaction is of essential importance, otherwise the in-plane flow is mostly overpredicted. The use of Dirac-Brueckner fields is, however, only reliable below about 1 GeV/nucleon as seen from a comparison to the empirical nucleon-nucleus optical potential. This limitation is reflected in the analysis of in-plane flow observables where the agreement with the data is best below 800 A.MeV. The calculations with the more weakly repulsive non-linear $\sigma\omega$ model (NL2) generally underestimate the in-plane flow. This demonstrates that the reaction dynamics is governed mainly by the repulsive momentum dependence of the nuclear fields and less so by the density dependence in the compression phase. The in-plane flow of light fragments further opens the possibility to test the model at low densities since the fragment formation mainly takes place in the decompression phase. However, in this study the flow of fragments does not lead to decisive results. One reason may be the simple theoretical description of the fragment formation. On the other hand, the DB forces used in the present calculations were extrapolated into the low density regime and thus are not very reliable there. Future investigations of the fragment flow might be able to set constraints on the low density behavior of the nuclear mean field. Recent DB calculations performed by the Tübingen Group [5,6] with

the Bonn potentials would be interesting to study in future applications.

The out-of-plane dynamics are found to be more difficult to interpret. The squeeze-out effect is qualitatively reproduced by both models but also substantial differences are seen. The azimuthal emission patterns which reflect the transition from in-plane to out-of-plane flow in more detail only yield a qualitative description of the data. It will be a challenge for future investigation to improve on this, most likely by the consistent inclusion of in-medium cross sections. However, also here the description becomes worse when non-equilibrium effects are neglected showing an unrealistic overprediction of the squeeze-out.

In summary, the present analysis of in-plane and out-of-plane observables with microscopic and phenomenological fields and the comparison to experimental data can be discussed in two ways: Firstly, there are substantial differences in the description between using the LDA and LCA approximations, both based on the same DB calculations, i.e. on the same EOS. Therefore non-equilibrium effects are important in the mean field of heavy ion collisions and the EOS can only be extracted reliably by taking these into account. Secondly, the calculations with microscopic fields - including non-equilibrium effects - describe the data generally well enough, usually better than with phenomenological fields. From this we may conclude that microscopic nuclear fields can be expected to describe nuclear systems not only for nuclear matter and finite nuclei in equilibrium, but also in the highly non-equilibrated situation of heavy ion collisions. Thus one can expect to move towards a unification of the description of very different nuclear systems and to a determination of the EOS of nuclear matter. However, further systematic investigations are certainly necessary to corroborate this conclusion.

Acknowledgements

The authors would like to thank the FOPI group for providing us with the filter simulation code and the data shown in this work. In particular we thank P. Crochet for very helpful comments concerning the comparison to the data. Finally we would like to thank S. Typel for further helpful discussions.

References

- [1] C.J. Horowitz, B.D. Serot, Nucl. Phys. A 464 (1987) 613.
- [2] B. ter Haar, R. Malfliet, Phys. Rep. 149 (1987) 207.
- [3] B. ter Haar, R. Malfliet, Phys. Rev. C 36 (1987) 1611.
- [4] R. Brockmann, R. Machleidt, Phys. Rev. C 42 (1990) 1965.
- [5] L. Sehn, C. Fuchs, Amand Faessler, Phys. Rev. C 56 (1997) 216.
- [6] C. Fuchs, T. Waindzoeh, Amand Faessler, and D.S. Kosov, Phys. Rev. C 58 (1998) 2022.
- [7] R. Machleidt, Advances in Nuclear Physics 19 (1989) 189.
- [8] H.F. Boersma, R. Malfliet, Phys. Rev. C 49 (1994) 233;
Phys. Rev. C 49 (1994) 1495.
- [9] H. Lenske, C. Fuchs, Phys. Lett. B 345 (1995) 355.
- [10] C. Fuchs, H. Lenske, H.H. Wolter, Phys. Rev. C 52 (1995) 3043.
- [11] C. Fuchs, T. Gaitanos, H. H. Wolter, Phys. Lett. B 381 (1996) 23.
- [12] C. Fuchs, P. Essler, T. Gaitanos, H. H. Wolter, Nucl. Phys. A 626 (1997) 987.
- [13] C. Fuchs, L. Sehn, H.H. Wolter, Nucl. Phys. A 545 (1992) 151c.
- [14] C. Gregoire, B. Remaud, F. Seville, L. Vincet, and Y. Raffay, Nucl. Phys. A 465 (1987) 317.
- [15] G.F. Bertsch and S. Das Gupta, Phys. Rep. 160 (1988) 190.
- [16] B.D. Serot and J.D. Walecka, in Advances of Nuclear Physics, Ed. J.W. Negele and E. Vogt, (Plenum Press, New York, 1986), Vol.16, S. 1.
- [17] P. Ring, Prog. Part. Nucl. Phys. 78 (1996) 193.
- [18] T.H. Elze, M. Gyulassy, D. Vasak, H. Heinz H. Stöcker and W. Greiner, Mod. Phys. Lett. 2A (1987) 451.

- [19] B. Blättel, V. Koch, U. Mosel, Rep. Prog. Phys. 56 (1993) 1.
- [20] Guangjun Mao, L. Neise, H. Stöcker, W. Greiner, Zhuxia Li, Phys. Rev. C in press.
- [21] C. Fuchs, H.H. Wolter, Nucl. Phys. A 589 (1995) 732.
- [22] P. Danielewicz, Ann. Phys. (NY) 152 (1984) 239.
- [23] W. Botermans, R. Malfliet, Phys. Rep. 198 (1990) 115.
- [24] L. Sehn, H.H. Wolter, Nucl. Phys. A 519 (1990) 289c.
- [25] L. Sehn, H.H. Wolter, Nucl. Phys. A 601 (1996) 473.
- [26] C. Fuchs, L. Sehn, H. H. Wolter, Nucl. Phys. A 601 (1996) 505.
- [27] W. Reisdorf and the FOPI Collaboration, Nucl. Phys. A 612 (1997) 493.
- [28] J. Aichelin, H. Stöcker, Phys. Lett. B 176 (1986) 14.
- [29] J. Aichelin, Phys. Rep. 202 (1991) 233.
- [30] K. Weber, B. Blättel, W. Cassing, H.C. Dönges, V. Koch, A. Lang and U. Mosel, Nucl. Phys. A 539 (1992) 713.
- [31] P. Dupieux and the FOPI Collaboration, Nucl. Phys. A 587 (1995) 802.
- [32] T. Maruyama, W. Cassing, U. Mosel, S. Teis and K. Weber, Nucl. Phys. A 573 (1994) 653.
- [33] P.K. Sahu, A. Hombach, W. Cassing, and, U. Mosel, Nucl. Phys. A 640 (1998) 493.
- [34] G.Q. Li and R. Machleidt, Phys. Rev. C 48 (1993) 1702.
- [35] T. Alm, G. Röpke, M. Schmidt, Phys. Rev. C 50 (1994) 31.
- [36] J. Jaenicke, J. Aichelin, N. Ohtsuka, R. Linden, A. Faessler, Nucl. Phys. A 536 (1992) 201.
- [37] A. Bohnet, N. Ohtsuka, J. Aichelin, R. Linden, A. Faessler, Nucl. Phys. A 494 (1989) 349.

- [38] D.T. Khoa, N. Ohtsuka, M.A. Matin, A. Faessler, S.W. Huang, E. Lehmann and R.K. Puri, Nucl. Phys. A 548 (1992) 102.
- [39] C. Fuchs, E. Lehmann, R. Puri, L. Sehn, Amand Faessler, H.H. Wolter, J. Phys. G 22 (1996) 131.
- [40] E. Lehmann, Amand Faessler, J. Zipprich, Rajeev Puri, S. W. Huang, Z. Phys. A 355 (1996) 55.
- [41] V.S. Uma Maheswari, C. Fuchs, A. Faessler, L. Sehn, D. Kosov, Z.S. Wang, Nucl. Phys. A 628 (1998) 669.
- [42] N. Bastid and the FOPI Collaboration, Nucl. Phys. A 622 (1997) 573.
- [43] P. Crochet and the FOPI Collaboration, Nucl. Phys. A 624 (1997) 755.
- [44] P. Crochet and the FOPI Collaboration, Nucl. Phys. A 627 (1997) 522.
- [45] P. Crochet and the FOPI Collaboration, in XXXIV International Winter Meeting of Nuclear Physics, Bormio, Italy, 1996, ed. I. Iori, Univ. di Milano.
- [46] P. Danielewicz et al., Phys. Rev. C 38 (1988) 120.
- [47] S. Hama, B.C. Clark, E.D. Cooper, H.S. Sherif, R.L. Mercer, Phys. Rev. C 41 (1990) 2737.
- [48] P.C. Martin and J. Schwinger, Phys. Rev. 115 (1959) 1342.
- [49] P. Henning, Phys. Rep. 253 (1995) 235.
- [50] R. Fauser, H.H. Wolter, Nucl. Phys. A 584 (1995) 604.
- [51] J. Knoll D.N. Voskrensky, Ann. Phys. (N.Y.) 249 (1996) 532.
- [52] J. Cugnon, T. Mizuani and J. Vandermeulen, Nucl. Phys. A 352 (1981) 505.
- [53] J. Boguta and A.R. Bodmer, Nucl. Phys. A 292 (1977) 413; J. Boguta and H. Stöcker, Phys. Lett. B 120 (1983) 289.
- [54] C. Fuchs, E. Lehmann, L. Sehn, F. Scholz, J. Zipprich, T. Kubo, and Amand Faessler, Nucl. Phys. A 603 (1996) 471.

- [55] C. M. Ko and G. Q. Li, *J. Phys. G* 22 (1996) 1673.
- [56] L. Sehn, A. Faessler, C. Fuchs, *J. Phys. G* 24 (1998) 135.
- [57] Gy. Wolf, G. Batko, W. Cassing, U. Mosel and M. Schäfer, *Nucl. Phys. A* 517 (1990) 615.
- [58] S. Ayik, C. Gregoire, *Nucl. Phys. A* 513 (1990) 187.
 J. Randrup, B. Remaud, *Nucl. Phys. A* 514 (1990) 339.
 Y. Abe, S. Ayik, P. G. Reinhard, E. Suraud, *Phys. Rep.* 275 (1996) 49.
- [59] M. Colonna, M. Di Toro, A. Guarnera, V. Latora, A. Smerzi, *Phys. Lett. B* (1993) 273.
- [60] M. Colonna, M. Di Toro, S. Maccarone, M. Zielinska-Pfabe, A. Guarnera, *Proc. of CRIS 1996, Acicstello, Italy*, ed. S. Costa et al., World Scientific 1996;
 M. Colonna, M. Di Toro, A. Guarnera, S. Maccarone, M. Zielinska-Pfabe, H. H. Wolter, *Nucl. Phys. A* (1998) in print.
- [61] J. I. Kapusta, *Phys. Rev. C* 21 (1980) 1301.
- [62] H. Sato, K. Yazaki, *Phys. Lett. B* 98 (1981) 153.
- [63] J. P. Bondorf, S. I. A. Garpman, J. Zimanyi, *Nucl. Phys. A* 296 (1978) 320.
- [64] P. Crochet, PhD Thesis, University Strasbourg (1996).
- [65] P. Crochet, private communication.
- [66] W. Reisdorf (FOPI Collaboration), private communication.
- [67] G. Peilert, H. Stöcker, W. Greiner, A. Rosenhauer, A. Bohnet, J. Aichelin, *Phys. Rev. C* 39 (1989) 1402.
- [68] P. B. Gossiaux, R. Puri, Ch. Hartnack, J. Aichelin, *Nucl. Phys. A* 619 (1997) 379.
- [69] W. Reisdorf and H.G. Ritter, *Annu. Rev. Nucl. Part. Sci.* 47 (1997) 663.
- [70] J. Kapusta and D. Strottman, *Phys. Lett. B* 106 (1981) 33.

- [71] H. Stöcker, L.P. Csernai, G. Graebner, G. Buchwald, H. Kruse, R.Y. Cusson, J.A. Mahrun, and W. Greiner, Phys. Rev. C 25 (1982) 1873.
- [72] H. H. Gutbrod, K. H. Kampert, B. W. Kolb, A. M. Poskanzer, H. G. Ritter, H. R. Schmidt, Phys. Lett. B 216 (1989) 267;
Phys. Rev. C42 (1990) 640.
- [73] M. Demoulin and the DIOGENE Collaboration, Phys. Lett. B 241 (1990) 476.
- [74] C. Hartnack et al., Phys. Lett. B 336 (1994) 131.
- [75] S. A. Bass et al., Z. Phys. A 352 (1995) 171.

	DB	NL2	NL3
BE [<i>MeV</i>]	-13.65	-16	-16
ρ_{sat} [<i>fm</i> ⁻³]	0.163	0.145	0.145
K^{-1} [<i>MeV</i>]	250	200	380
m^*/M	0.58	0.83	0.70

Table 1

Nuclear matter bulk properties for the non-linear Walecka model in the NL2 and NL3 parametrisation [19] and for the microscopic DB approach [2].

$ \mathbf{v} /c$	$\bar{\Gamma}_s^{(12)}$			$\bar{\Gamma}_0^{(12)}$		
	α_s	β_s	γ_s	α_0	β_0	γ_0
0.0	14.3824	5.9953	17.5509	10.9222	6.1806	13.526
0.1	17.1786	5.8245	17.7130	14.3573	6.3442	13.3728
0.2	16.9493	5.1213	17.6029	13.1190	5.2685	13.0947
0.3	16.3484	4.4216	17.2461	12.7487	4.4378	12.5720
0.4	14.4627	3.4204	16.5104	11.2137	3.2912	11.7113
0.5	12.9065	2.3405	15.1360	10.0609	1.9533	9.9478
0.6	12.2228	1.8107	14.0333	9.9916	1.3334	8.2921
0.7	10.5331	2.4902	15.4875	7.5123	2.2559	10.4210
0.8	10.5551	3.5655	16.1264	7.3937	3.7189	11.0364
0.9	11.4589	3.9925	15.6650	8.2575	4.5667	10.6923
0.99	12.0807	4.0514	15.0879	8.9602	4.9836	10.2812

Table 2

Coefficients $\alpha_{s,0}$, $\beta_{s,0}$ and $\gamma_{s,0}$ for the parameterization, Eq. (27), of the effective non-equilibrium DB vertex functions as functions of the c.m. nuclear matter streaming velocities

E_{beam}	250 A.MeV	400 A.MeV	600 A.MeV
FOPI	44	55	62
NL2	52	58	66
DB/LCA	50	52	58
DB/LDA	51	54	60

Table 3

Lower limits of the highest multiplicity bin PM5 in Au on Au reactions at various incident energies. The calculations are performed with DB forces including (DB/LCA) and without (DB/LDA) non-equilibrium effects and with the $\sigma\omega$ model (NL2). The corresponding experimental values (FOPI) are taken from Ref. [43].

E_{beam}		250 A.MeV	400 A.MeV	600 A.MeV
<i>PM3</i>	$\langle b_{\text{FOPI}} \rangle$	6.3	6.3	5.5
	$\langle b_{\text{NL2}} \rangle$	8.8	9.0	8.5
	$\langle b_{\text{DB/LCA}} \rangle$	6.5	8.6	8.6
<i>PM4</i>	$\langle b_{\text{FOPI}} \rangle$	4.2	4.1	3.4
	$\langle b_{\text{NL2}} \rangle$	5.3	5.3	5.1
	$\langle b_{\text{DB/LCA}} \rangle$	3.9	5.0	4.9
<i>PM5</i>	$\langle b_{\text{FOPI}} \rangle$	1.8	1.6	1.2
	$\langle b_{\text{NL2}} \rangle$	2.0	1.3	2.0
	$\langle b_{\text{DB/LCA}} \rangle$	1.3	1.3	1.3

Table 4

Correlation between the mean impact parameter $\langle b \rangle$ [fm] and the multiplicity bins in Au on Au reactions at various incident energies. The calculations are performed with non-equilibrium DB forces (DB/LCA) and with the $\sigma\omega$ model (NL2). The corresponding experimental values (FOPI) are obtained in with sharp cutoff model [64].

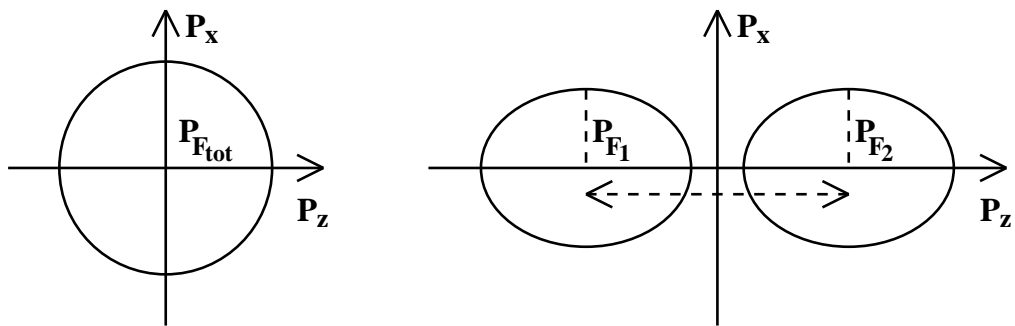


Fig. 1. Schematic representation of the local momentum space which corresponds to the local density approximation (left) and the local configuration approximation (right).

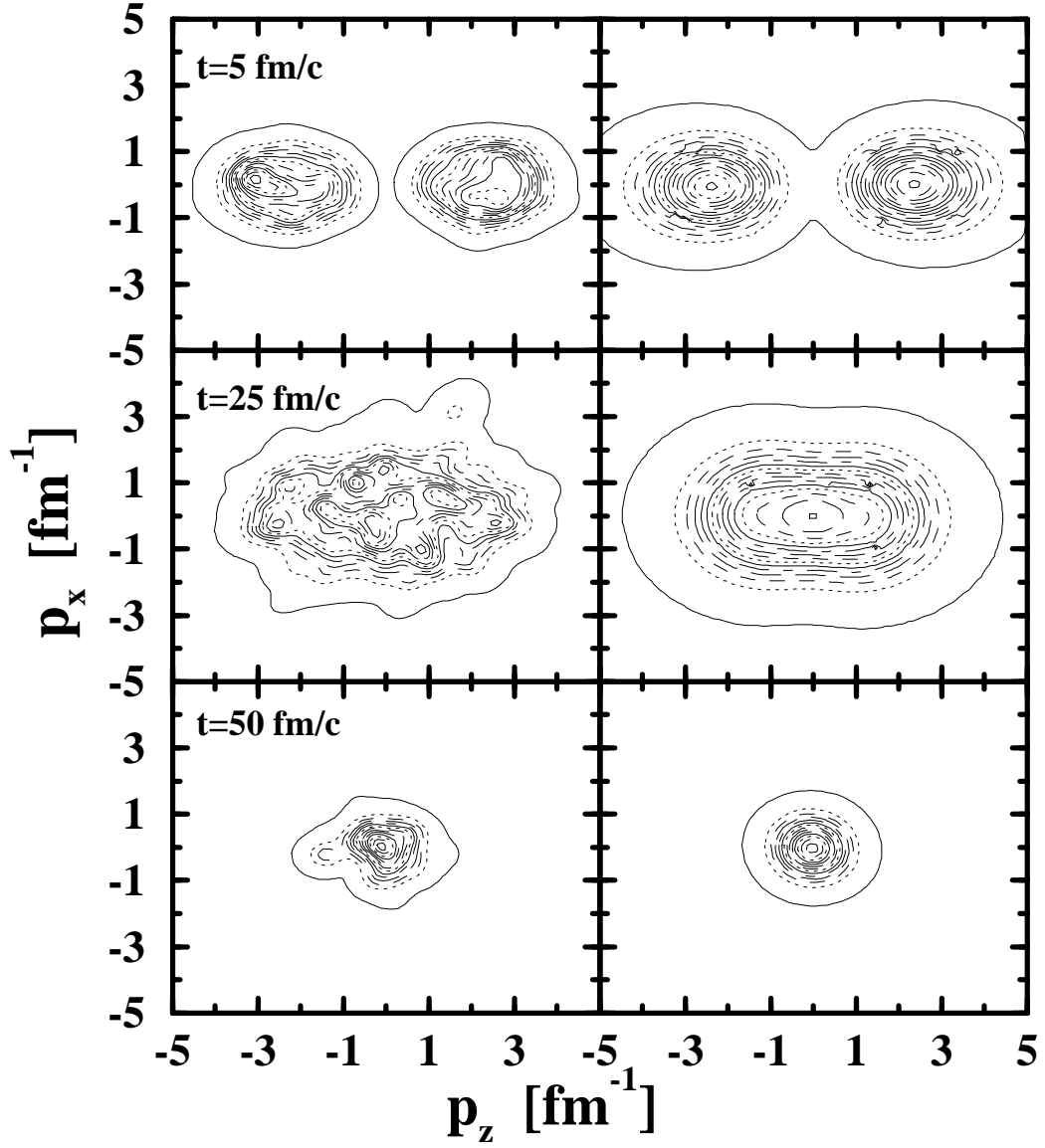


Fig. 2. Local momentum distributions obtained from the transport calculation (left columns) and the corresponding fitted two hot Fermi-sphere distributions (right columns) at different stages ($t = 5, 25$ and 50 fm/c) in the central region of a central ($b = 0$ fm) Au+Au reaction at 600 A.MeV.

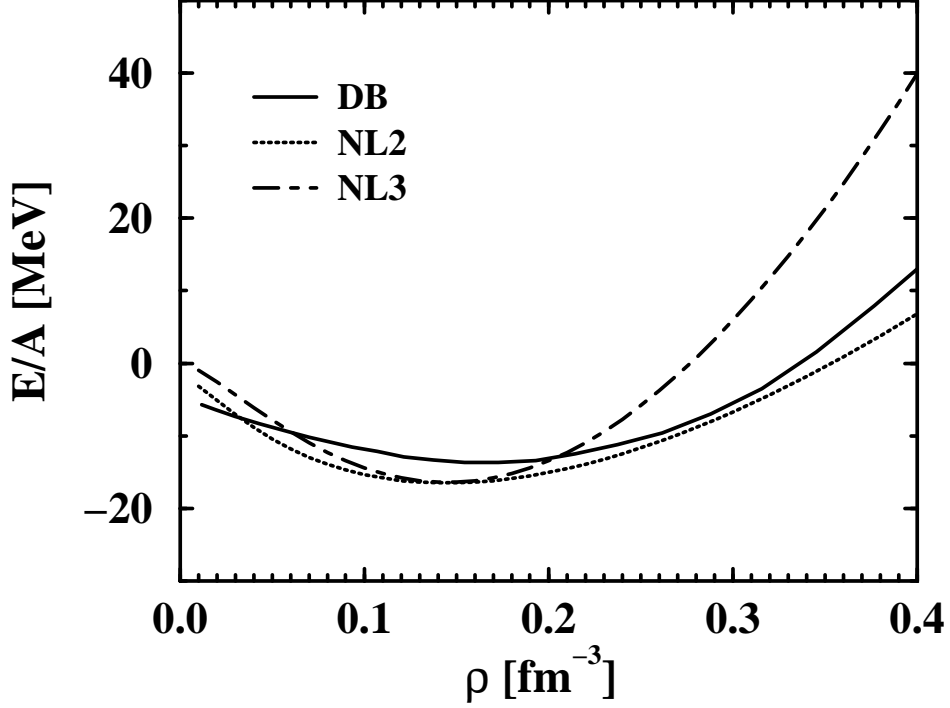


Fig. 3. Equation-of-state in the DB approach [2] and in the non-linear $\sigma\omega$ -model with parameter sets NL2 (soft) and NL3 (hard).

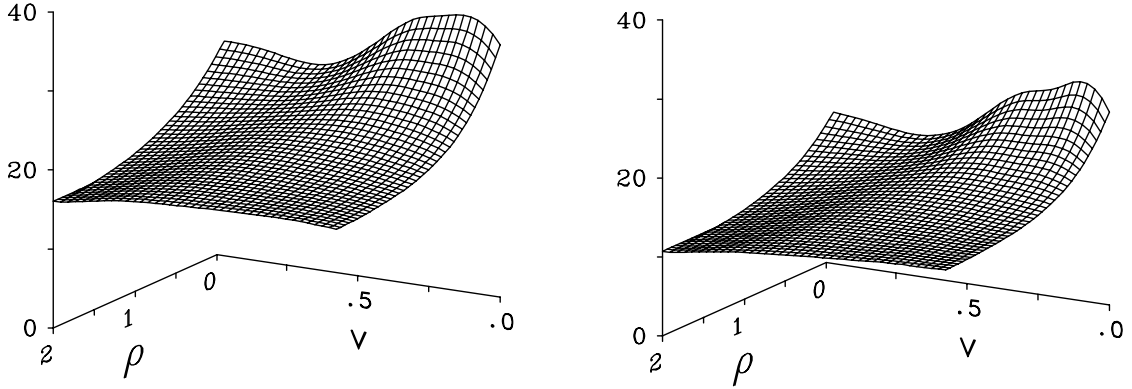


Fig. 4. Dynamical vertex functions $\bar{\Gamma}_s^{(12)}$ (left) and $\bar{\Gamma}_0^{(12)}$ (right) in symmetric colliding nuclear matter as functions of the subsystem density $\rho_0^{(i)}$ and the streaming velocity v of the subsystems in dimensionless units ($\times \frac{M^2}{4\pi}$).

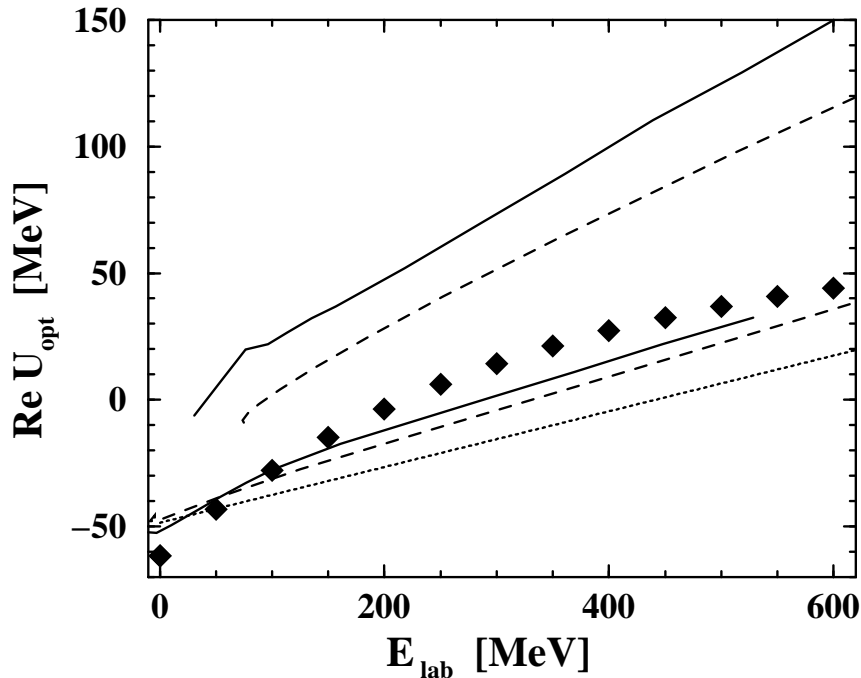


Fig. 5. Energy dependence of different optical potentials. The solid lines represent the DB nucleon–nucleus optical potential [2] at saturation density ρ_{sat} (lower curve) and $2\rho_{\text{sat}}$ (upper curve). The dashed lines represent the corresponding nucleon optical potential in a nucleus–nucleus collision determined in the colliding nuclear matter approximation at subsystem densities $\rho_0^{(1)} + \rho_0^{(2)} = \rho_{\text{sat}}$ (lower curve) and $\rho_0^{(1)} + \rho_0^{(2)} = 2\rho_{\text{sat}}$ (upper curve). The dotted line refers to the nucleon–nucleus optical potential at ρ_{sat} in the non–linear $\sigma\omega$ –model NL2, and the diamonds are the corresponding empirical values [47].

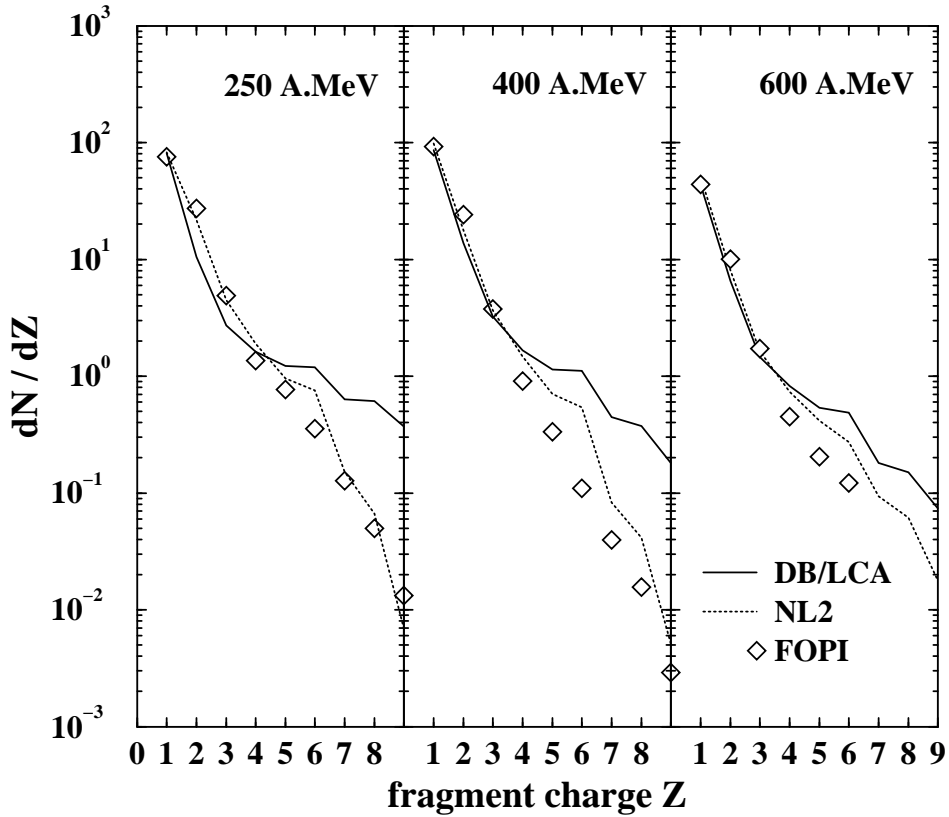


Fig. 6. Comparison of the theoretical charge distributions to the FOPI data [27] for central Au+Au reactions at 250 (left), 400 (middle) and 600 A.MeV (right). The solid and dotted lines represent the charge distributions determined in the DB/LCA and NL2 models, respectively. At 250 and 400 A.MeV the centrality class was determined by the *ERAT* selection with the corresponding *ERAT*-bins taken from Ref. [27]. At 600 A.MeV the *PM4* selection was used (see section 6.1).

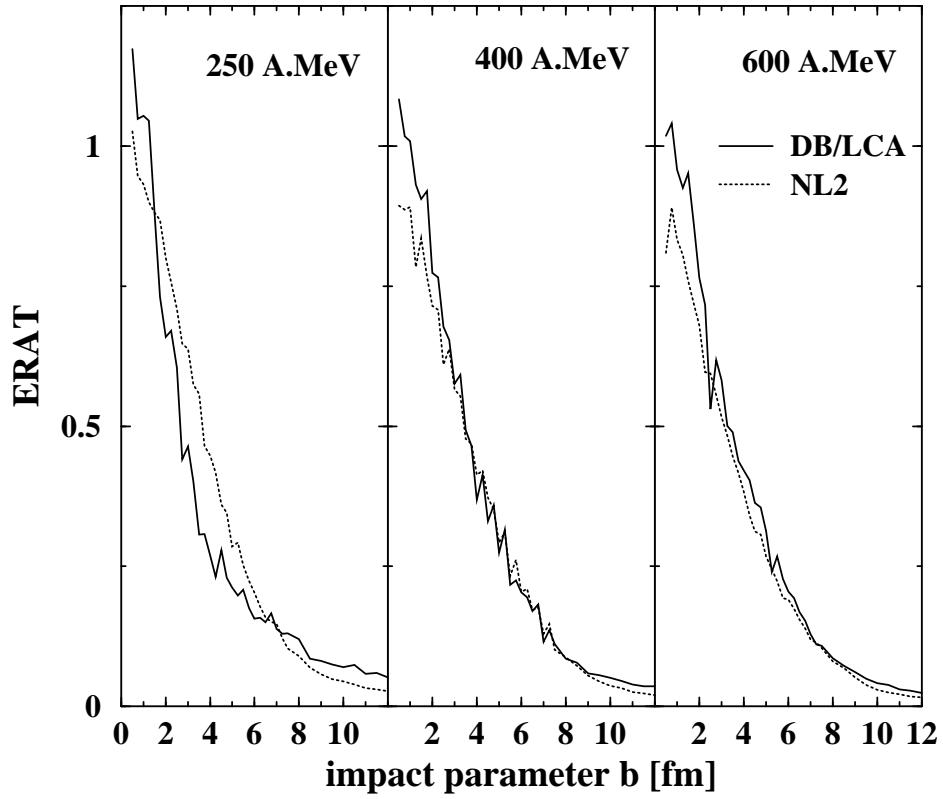


Fig. 7. Correlation between the observable $ERAT$ and the impact parameter for Au+Au reactions at 250 (left), 400 (middle) and 600 A.MeV (right). The curves have the same meaning as in Fig. 6.

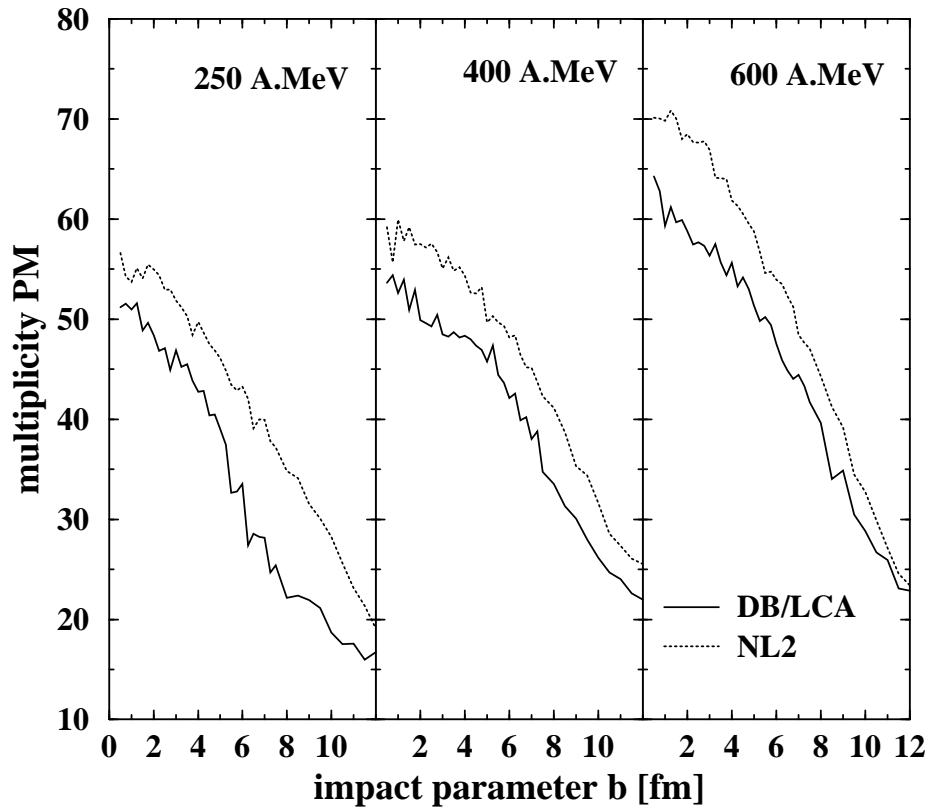


Fig. 8. Correlation between the mean multiplicity PM and the impact parameter for Au+Au reactions at 250 (left), 400 (middle) and 600 A.MeV (right). The curves have the same meaning as in Fig. 6.

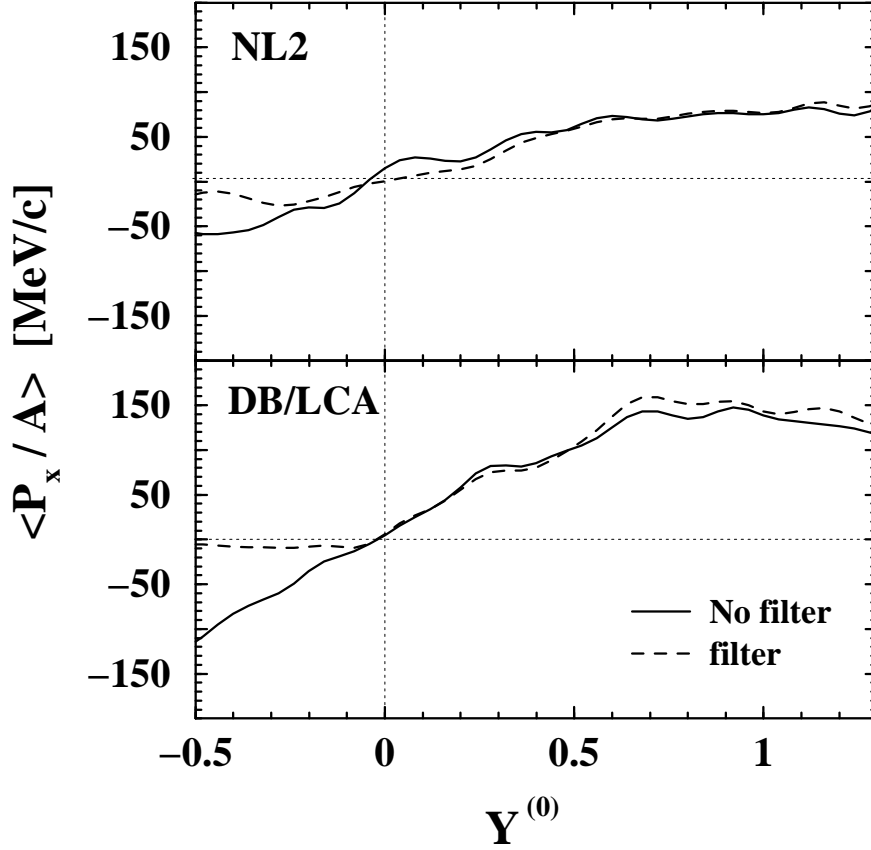


Fig. 9. Mean in-plane flow $\langle p_x / A \rangle$ in a semi-central ($b = 3$ fm) Au+Au reaction at 600 A.MeV. The model dependence and the influence of the FOPI filter on the sideward flow is shown. The solid lines represent the unfiltered, the dashed lines the filtered results obtained in the NL2 (top) and DB/LCA (bottom) model, respectively.

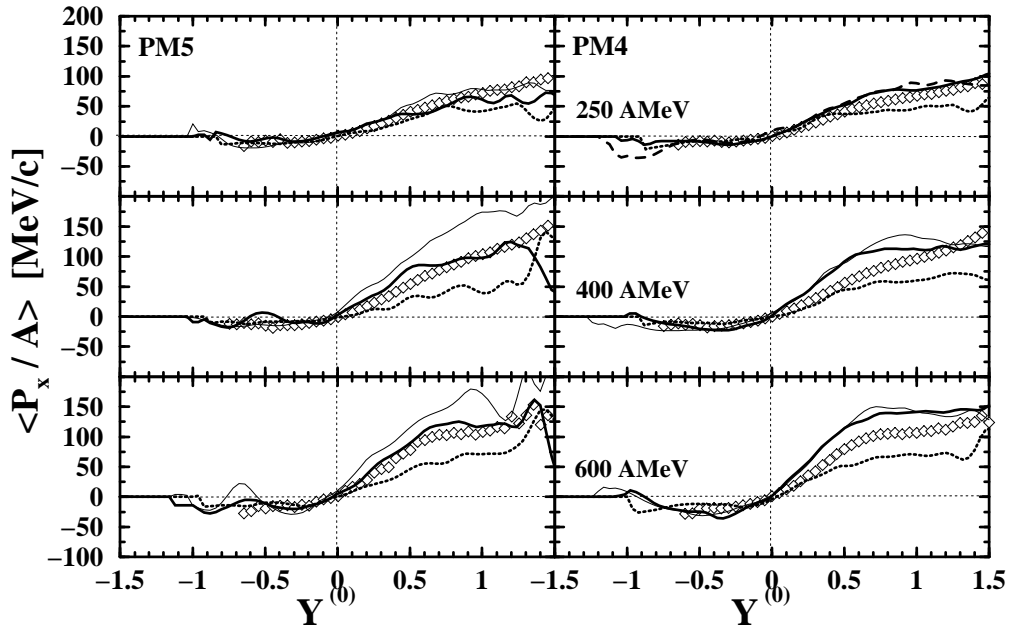


Fig. 10. Comparison of the sideward flow of protons ($Z = 1$) with the FOPI data (diamonds) taken from [64,65]. The calculations are performed in the DB model with (DB/LCA, solid) and without non-equilibrium effects (DB/LDA, dashed) and in the non-linear $\sigma\omega$ model NL2 (dotted). The left panels correspond to central (PM5), the right panels to peripheral (PM4) Au on Au reactions at different beam energies of 250 (top), 400 (middle) and 600 (bottom) A.MeV.

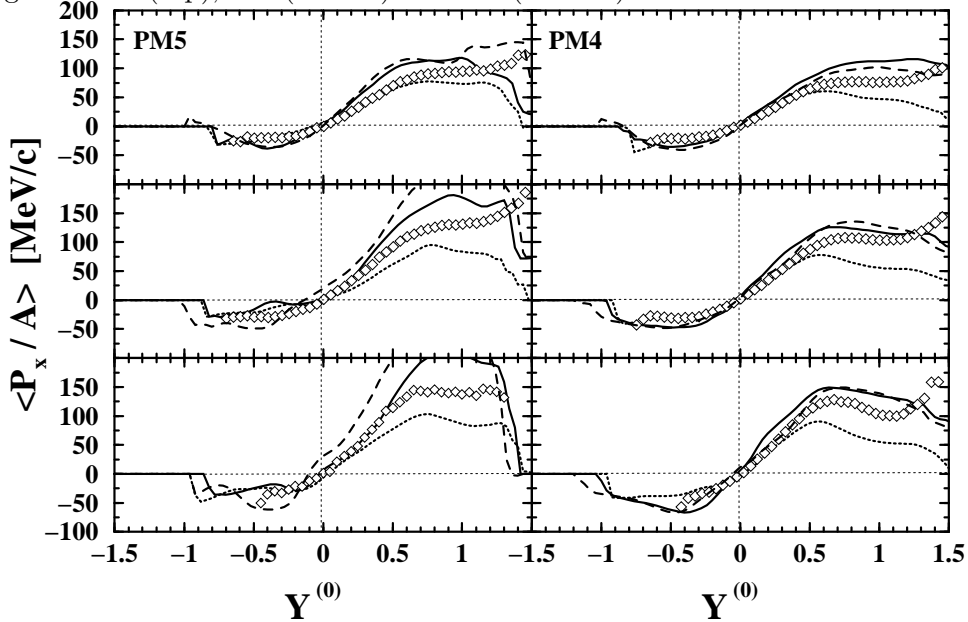


Fig. 11. Comparison of the (filtered) sideward flow per nucleon of fragments with charge $Z = 2$ with the FOPI data (diamonds) taken from [64,65]. The curves have the same meaning as in Fig. 10.

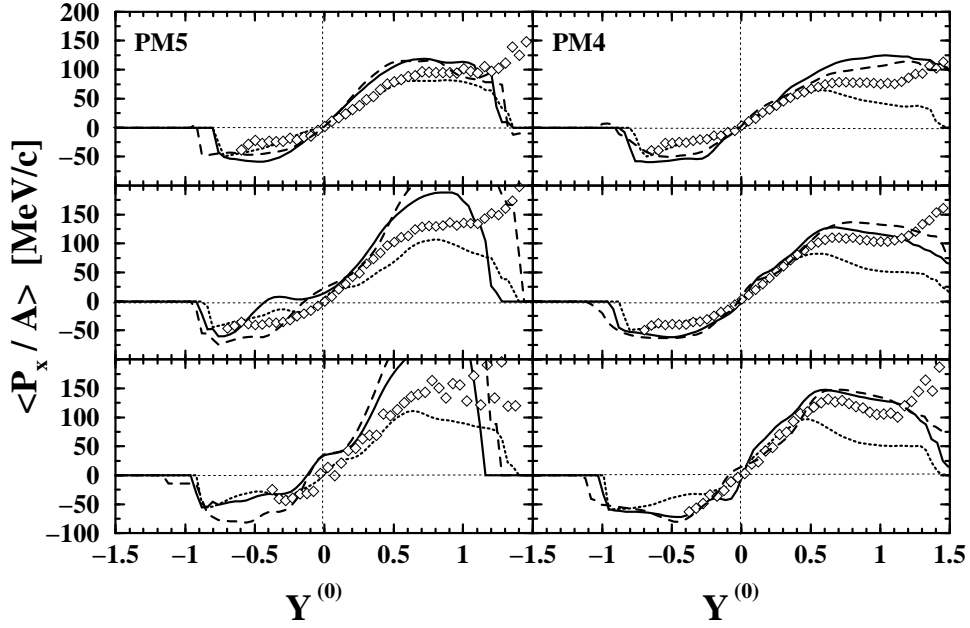


Fig. 12. Comparison of the sideward flow per nucleon of fragments with charge $Z = 3$ with the FOPI data (diamonds) taken from [64,65]. The curves have the same meaning as in Fig. 10.

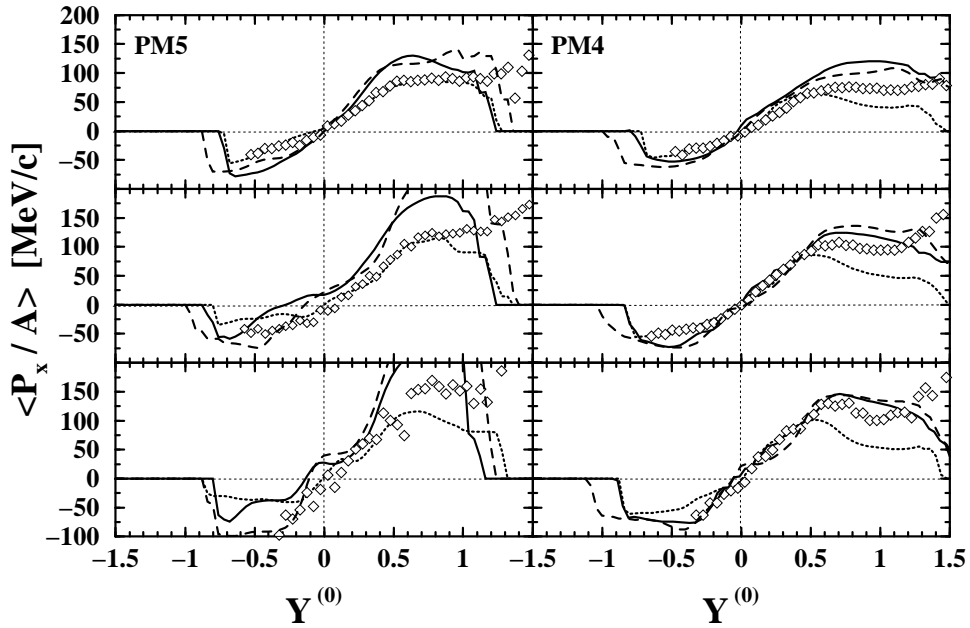


Fig. 13. Comparison of the sideward flow per nucleon of fragments with charge $Z = 4$ with the FOPI data (diamonds) taken from [64,65]. The curves have the same meaning as in Fig. 10.

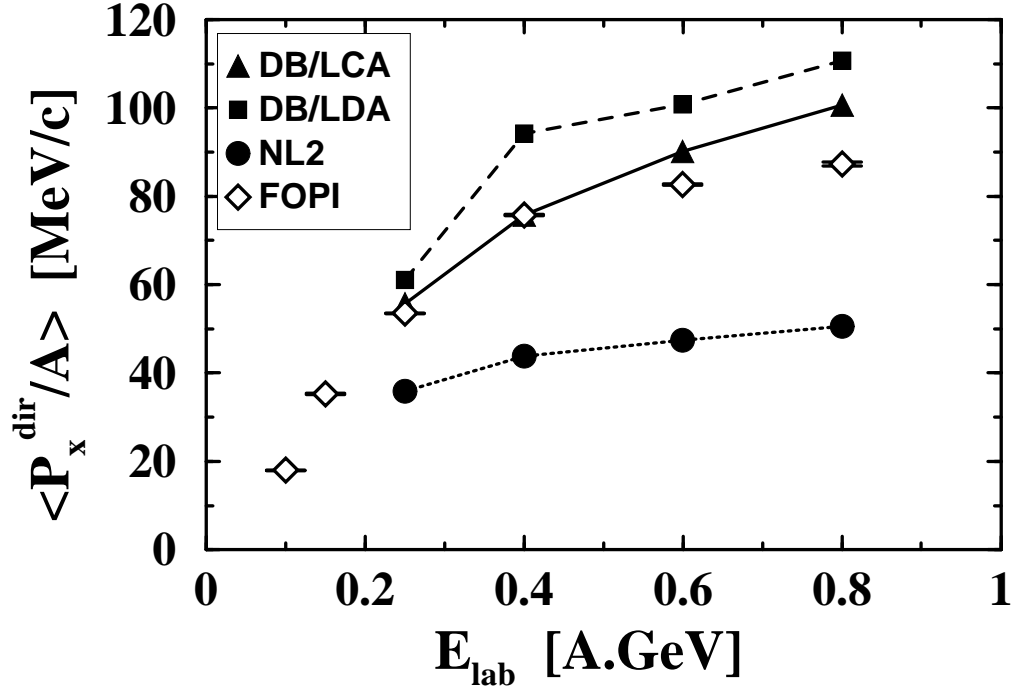


Fig. 14. Mean directed in-plane sideward flow per nucleon in semi-central ($PM4$) Au on Au reactions as a function of the beam energy. Calculations performed with DB model including (DB/LCA, triangles) and without non-equilibrium effects (DB/LDA, squares) and with the non-linear $\sigma\omega$ model NL2 (circles) are compared to the FOPI data (diamonds) taken from Ref. [64,65].

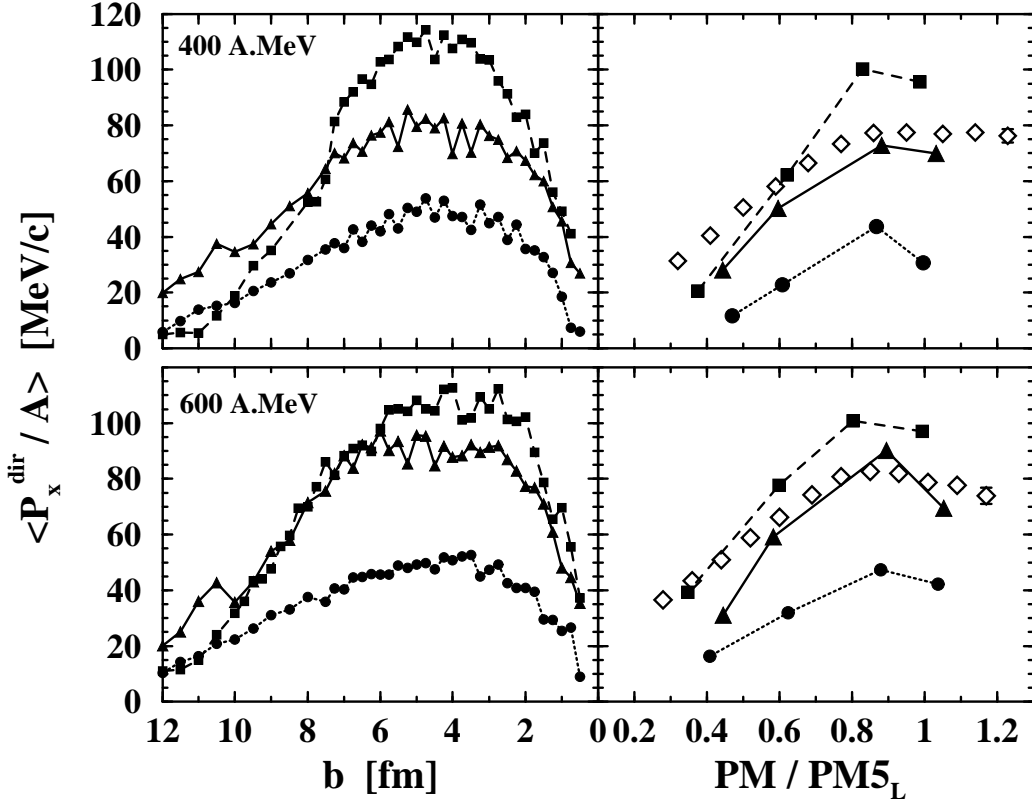


Fig. 15. Centrality dependence of the mean directed in-plane flow per nucleon for the system Au on Au at 400 (top panels) and 600 (bottom panels) A.MeV. The left panels show the impact parameter dependence of the calculation; on the right panels the calculations using the multiplicity selection are compared to the FOPI data [64,65]. Triangles refer to DB/LCA, squares to DB/LDA and circles to NL2.

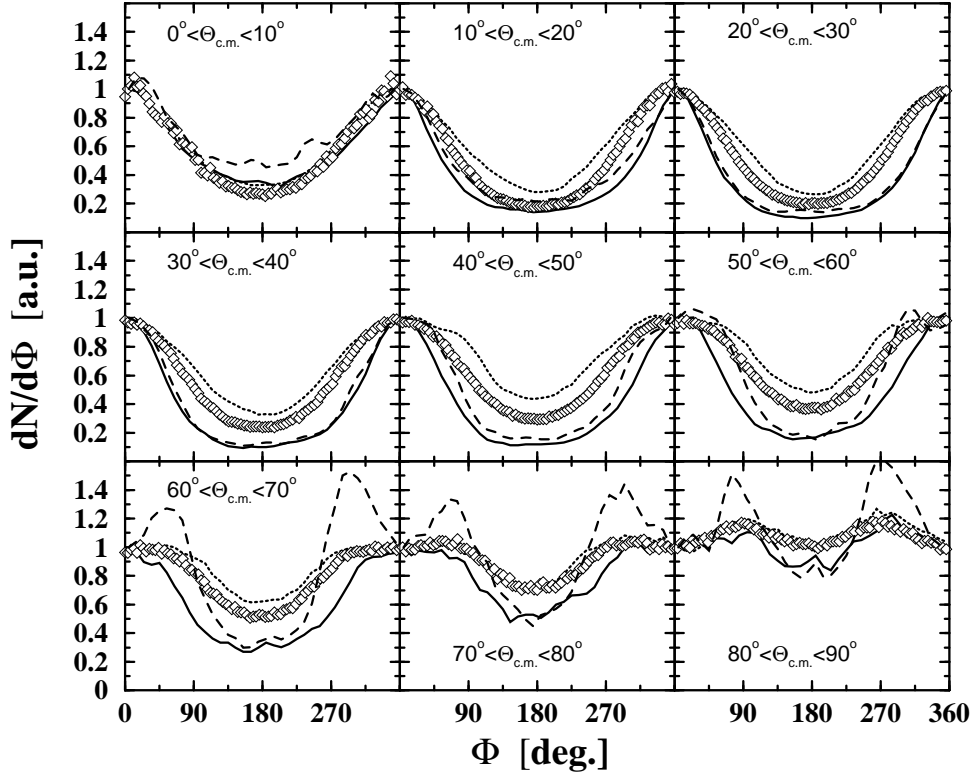


Fig. 16. Azimuthal distributions at different polar angles $\Theta_{c.m.}$ for a semi-central Au on Au reaction at 600 A.MeV. The calculations are performed within the DB model including (DB/LCA, solid) and without (DB/LDA, dashed) non-equilibrium effects and the non-linear $\sigma\omega$ model NL2 (dotted). The diamonds represent the data taken from Ref. [44].

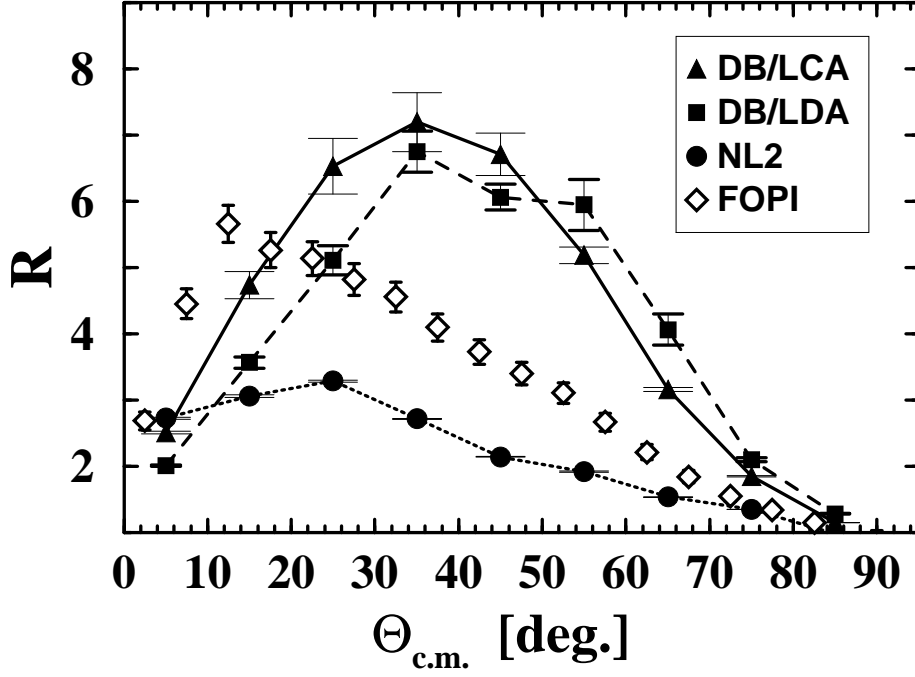


Fig. 17. Dependence of the in-plane emission, i.e. the azimuthal anisotropy ratio R , Eq. (36), on the c.m. polar angle in a semi-central Au on Au reaction at 600 A.MeV. The calculations are performed within the DB model including (DB/LCA, solid) and without (DB/LDA, dashed) non-equilibrium effects and the non-linear $\sigma\omega$ model NL2 (dotted). The diamonds refer to the FOPI data of Ref. [44].

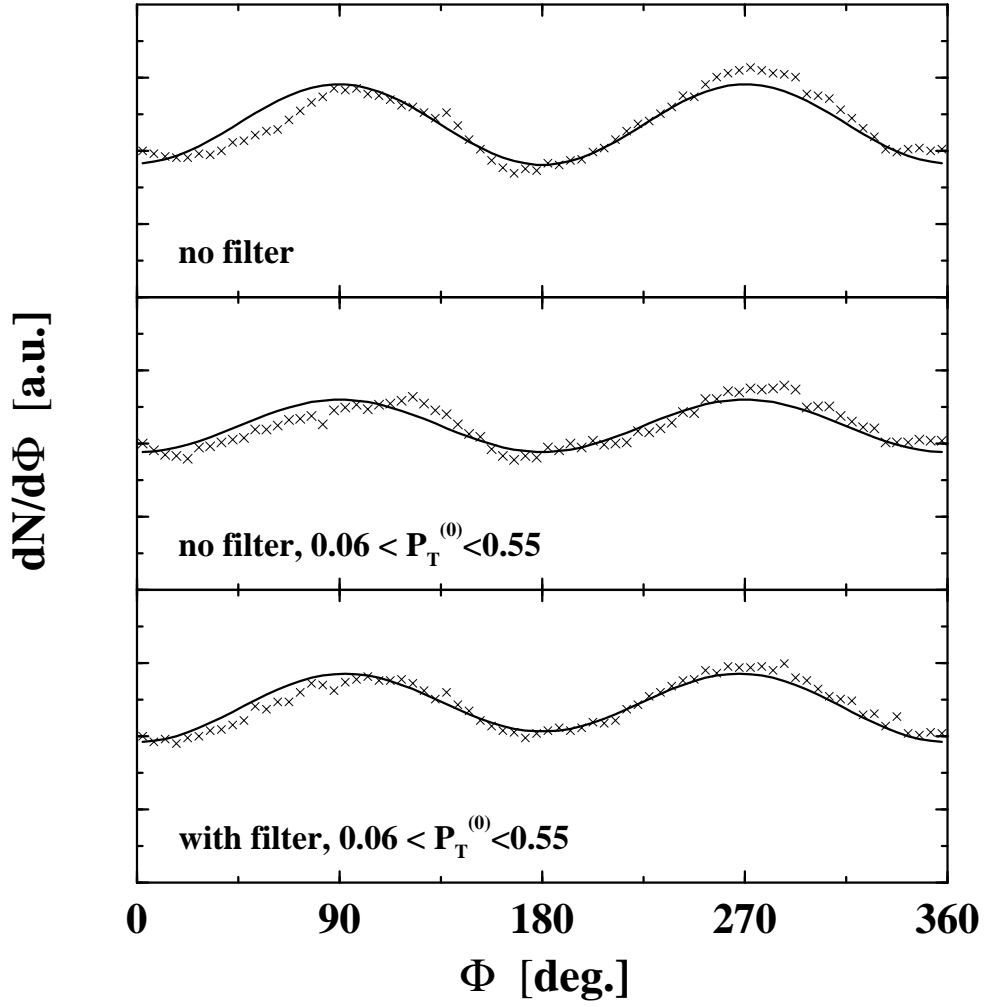


Fig. 18. Influence of the FOPI filter on the azimuthal distributions for a semi-central ($PM4$) Au on Au reaction at 600 A.MeV. The calculations are performed with the NL2 model. The solid lines are fits to the curves according to Eq. (37).

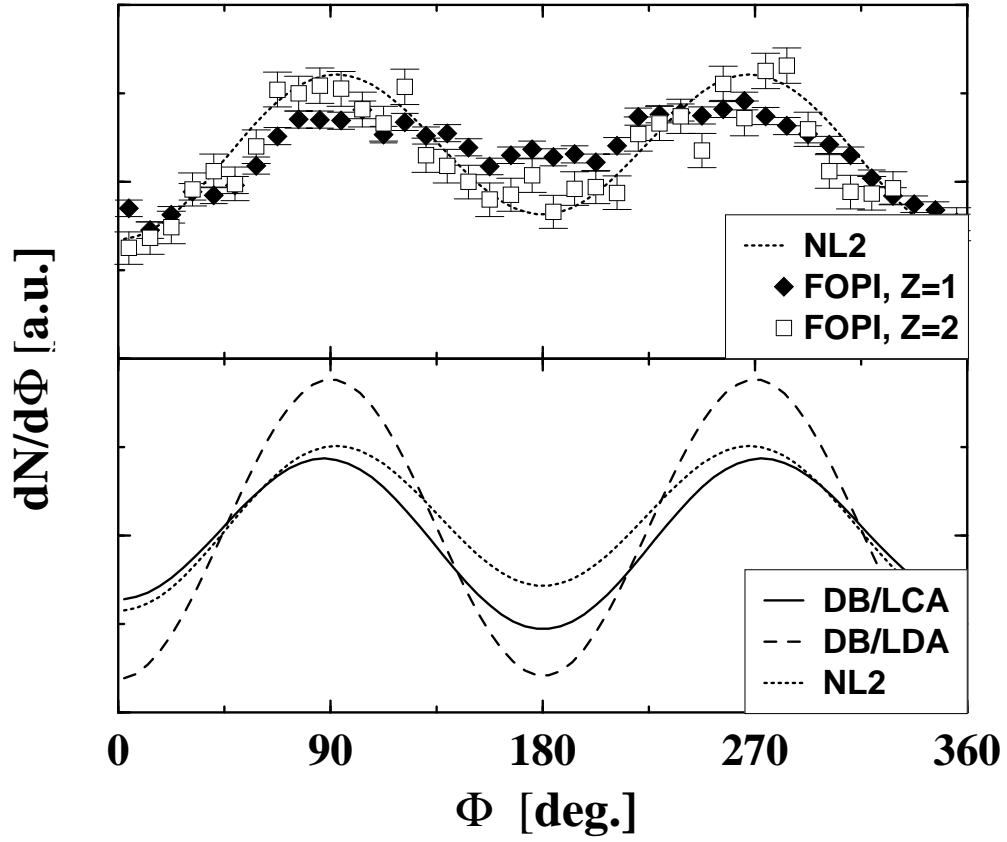


Fig. 19. Lower panel: Azimuthal distributions of protons ($Z = 1$) in a semi-central ($PM4$) Au on Au reaction at 600 A.MeV. The calculations are performed with the DB/LCA, DB/LDA and the NL2 forces. Upper panel: The NL2 results are compared to the corresponding FOPI data [45] for $Z = 1$ and $Z = 2$.

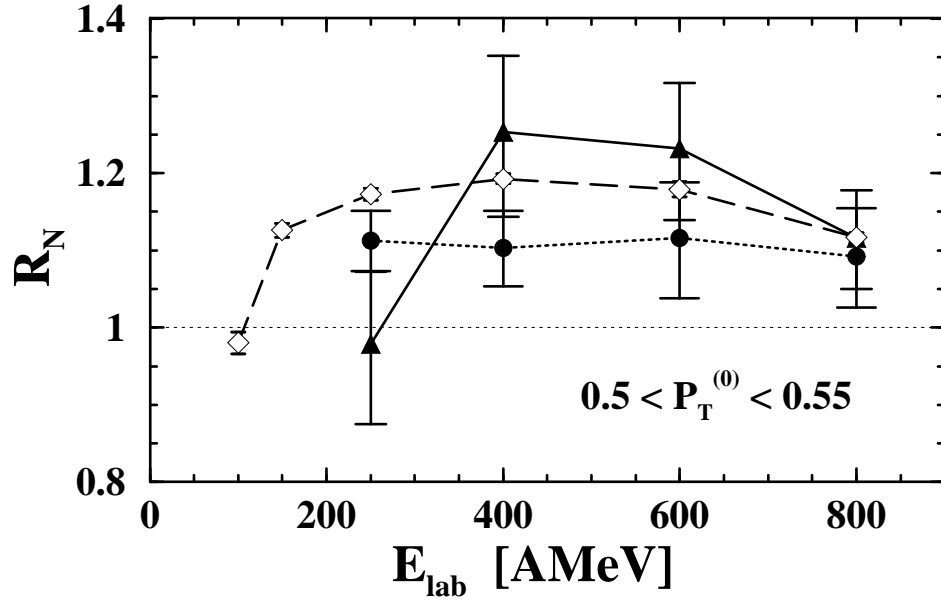


Fig. 20. Squeeze-out ratio R_N as a function of the incident energy for semi-central ($PM4$) Au on Au reactions with a $0.5 \leq P_T^{(0)} \leq 0.55$ cut. The theoretical calculations for the NL2 (circles) and the non-equilibrium DB forces (triangles) are shown and compared to the FOPI data (open diamonds) taken from Ref. [64].

